THE JOURNAL OF PHYSICAL CHEMISTRY C

Article

pubs.acs.org/JPCC

Anomalously Strong Electric Near-Field Enhancements at Defect Sites on Au Nanoshells Observed by Ultrafast Scanning Photoemission Imaging Microscopy

Andrej Grubisic,[†] Shaunak Mukherjee,[‡,∥] Naomi Halas,*[,‡,§,∥] and David J. Nesbitt*[,†]

[†]JILA, University of Colorado and National Institute of Standards and Technology, and Department of Chemistry and Biochemistry, University of Colorado, Boulder, Colorado 80309, United States

[‡]Department of Chemistry, [§]Department of Electrical and Computer Engineering, and [∥]Laboratory for Nanophotonics, Rice University, 6100 Main Street, Houston, Texas 77005, United States

ABSTRACT: Multiphoton photoelectron emission from individual SiO_2 core−Au shell nanoparticles supported on an ITO substrate is studied with ultrafast scanning photoemission imaging microscopy. Higher than expected photoemission yields (~10^5-fold) and a strong sensitivity to excitation laser polarization direction indicate the presence of anomalously high electromagnetic field enhancement areas (i.e., "hot spots") on the surface of Au nanoshells. The measured magnitude of the photoelectron current is consistent with 1−2 localized hot spots on each nanoparticle exhibiting electric near-field enhancement factors of nominally $|\mathbf{E}|/|\mathbf{E}_0| \sim 50-100$. Secondary electron microscopy (SEM) studies reveal asperities on the surface of each nanoparticle that most likely arise due to postsynthetic Ostwald ripening of the Au shell layer. However, no correlation is found between these features and the laser polarization that yields the maximum photoelectron emissivity, indicating that the hot spots responsible for the observed high electron emission rates are smaller than our SEM resolution of ~3−5 nm. Numerical electrodynamics simulations of near-field enhancements ($|\mathbf{E}|/|\mathbf{E}_0| \sim 20$) for the two most commonly observed defect geometries (i.e., asperities and pinholes) can account for <20−50% of the experimentally inferred values. The larger near-field enhancements observed experimentally thus provide indirect evidence for sharp asperities and crevices in Au nanoshells considerably below the optical diffraction limit.

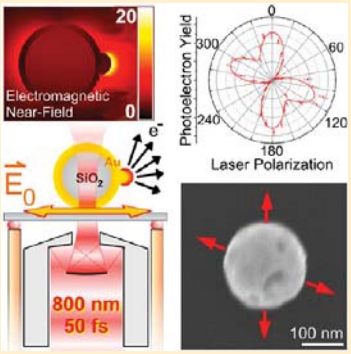

I. INTRODUCTION

Metallic nanoparticles (NPs) exhibit optical properties that can differ profoundly from those of the corresponding bulk metal; for example, resonances often exist in spectra of nanoparticles that are distinct from those determined purely by the electronic structure of the bulk material. These resonances arise due to the excitation of collective, coherent oscillations of conduction electrons known as localized surface plasmons (LSPs). The frequencies of LSP resonances depend sensitively on nanoparticle structure and can consequently be tuned over broad spectral ranges if the nanoparticle size, shape, and/or the surrounding medium are changed.[1−7] A rich variety of particle geometries can be readily synthesized (i.e., spheres,[8,9] rods,[10] cubes,[11] triangular prisms,[12] pentagonal bipyramids,[13] cages,[14] shells[15]), thus permitting an "off-the-shelf" nanoparticle system to be selected based on the specific optical response required by the envisioned application.

Silica−Au core−shell nanoparticles (i.e., Au nanoshells) have received considerable attention, due in part to the enormous success of Mie theory in predicting the relationship between their structure and optical properties.[15−17] Specifically, the plasmonic response of nanoshells is found to depend quite sensitively on the inner (r_1) and outer (r_2) radii of the metallic shell, with thinner shells resulting in a progressively more red-shifted dipolar plasmon resonance.[18] As a result, systematic variation of the shell layer thickness allows the dipolar resonance of the Au nanoshells to be tuned through most of the visible (vis) and well into the near-infrared (NIR) spectral range.[15] Such wide tunability makes Au nanoshells promising in a variety of applications, most notably solar energy conversion,[19−21] photothermal therapy,[22] as well as photoactivated drug and gene delivery.[23,24]

While scattering and absorption resonances represent *far-field* (observation distance $l \gg \lambda$) manifestations of the localized surface plasmon, the plasmon also profoundly influences the particle *near-field* ($l \ll \lambda$). In particular, the intensity of the incident electromagnetic radiation ($|\mathbf{E}_0|$) can be greatly amplified in the vicinity of plasmonic nanoparticles or nanostructures. The locally increased incident electric field ($|\mathbf{E}|$) is typically quantified in terms of a near-field enhancement factor $|\mathbf{E}|/|\mathbf{E}_0|$, with values of ~$10-10^2$ typically encountered in individual nanoparticles and as much as 10^3 in junctions between plasmonic particles.[25−29]

In general, nanoshell dimers would be expected to give rise to substantially stronger surface-enhanced Raman scattering (SERS) signals than single nanoshell particles, due to the

Received: July 25, 2013
Revised: October 2, 2013
Published: October 2, 2013

 © 2013 American Chemical Society dx.doi.org/10.1021/jp407424n | J. Phys. Chem. C 2013, 117, 22545−22559

considerably larger electromagnetic fields that can exist in nanometer-scale gaps between particles than on the surface of an individual nanoparticle.[30,31] In partial contrast to these expectations, however, previous work has revealed SERS activity of individual Au nanoshells to be in some cases comparable to that of Au nanoshell dimers.[32] This was interpreted to arise from unusually large near-field effects on Au nanoshells, with defects on the shell surface proposed to rationalize the anomalously large near-field enhancements inferred from SERS. These observations provided the motivation for the present study: to characterize the defects on nanoshell surfaces that generate high local electromagnetic fields and to elucidate whether the SERS enhancements may arise from a cumulative effect of a large number of defect sites or from very strong enhancements at only a few highly localized regions on the nanoparticle surface (i.e., "hot spots").

To address these questions, we have exploited scanning photoemission imaging microscopy (SPIM) to probe photoelectron emission from individual Au nanoshells upon ultrafast laser irradiation with photon energies ($E_{h\nu}$) below the metal work function (Φ).[33−36] Under these conditions, a minimum of $n > \Phi/E_{h\nu}$ photons is required energetically to eject an electron, with the multiphoton photoelectron emission (MPPE) rate[37−42] depending on $(|\mathbf{E}|/|\mathbf{E_0}|)^{2n}$. In the case of gold ($\Phi_{Au}$ = 4.7−5.1 eV),[43] n = 4 photons are required to emit a single electron at a typical excitation wavelength of $\lambda \sim 800$ nm ($E_{h\nu} \sim 1.5$ eV), thereby predicting a rapid $(|\mathbf{E}|/|\mathbf{E_0}|)^8$ dependence of the electron emission signal on laser field strength. Consequently, MPPE not only provides near-field information analogous to SERS (i.e., reporting on the local field enhancements) by an independent route, but also proves to be a remarkably sensitive tool for the identification of hot spots on metallic nanoparticles/structures, as recently demonstrated by a number of elegant studies.[35,36,44−47]

The inherent sensitivity of MPPE to local electromagnetic fields is exploited in the present study to detect the presence of hot spots on individual Au nanoshells, as well as to infer their specific location on the surface. The latter is achieved through measurements of nanoparticle photoemissivity as a function of excitation laser polarization. In previous studies, coplanar alignment of the laser polarization vector with the plane defined by the light propagation vector and the vector connecting the particle center to the hot spot is generally observed to result in strongest photoemission currents.[34−36] MPPE in such cases is a sensitive function of polarization angle θ, typically following a narrow $\cos^{2n}(\theta)$ angular distribution with $n \approx 4$, which allows the axis of the hot spot to be determined with a high precision. Such polarization-dependent photoemission data are then correlated with direct structural information obtained from secondary electron microscopy (SEM). These experimental findings are complemented with numerical simulations (COMSOL Multiphysics software package) of electromagnetic near fields around various putative structural features on Au nanoshells, to help identify specific morphological characteristics of hot spots on the Au nanoshell surfaces.

II. EXPERIMENTAL METHODS

Synthesis and Characterization. SiO_2 core−Au shell particles are synthesized via previously described methods.[15,48] Briefly, commercially available $\langle d \rangle$ = 160 nm diameter silica nanoparticles (Precision Colloids, Inc.) are functionalized with 3-aminopropyltriethoxysilane (Gelest, Inc.). Ultrasmall Au colloids are grown by a method described by Duff et al. and aged at 4 °C for two weeks.[49] The functionalized SiO_2 particles are then added to the Au colloid suspension, whereby the colloids covalently attach to the terminal amine groups on the silica surface and thus form seed particles. Complete Au nanoshells on the SiO_2 surface are obtained by an electroless plating technique, whereby seeds react with $HAuCl_4 \cdot 3H_2O$ in the presence of CO. Au^{3+} ions are reduced and deposited onto the surface of the seeds, thus forming a complete Au shell with its thickness controlled by the amount of CO added.

Extinction spectra of Au nanoshell aqueous solutions are recorded with a Cary 5000 UV−vis spectrometer and are shown in Figure 1 (top; solid line). Peaks corresponding to the

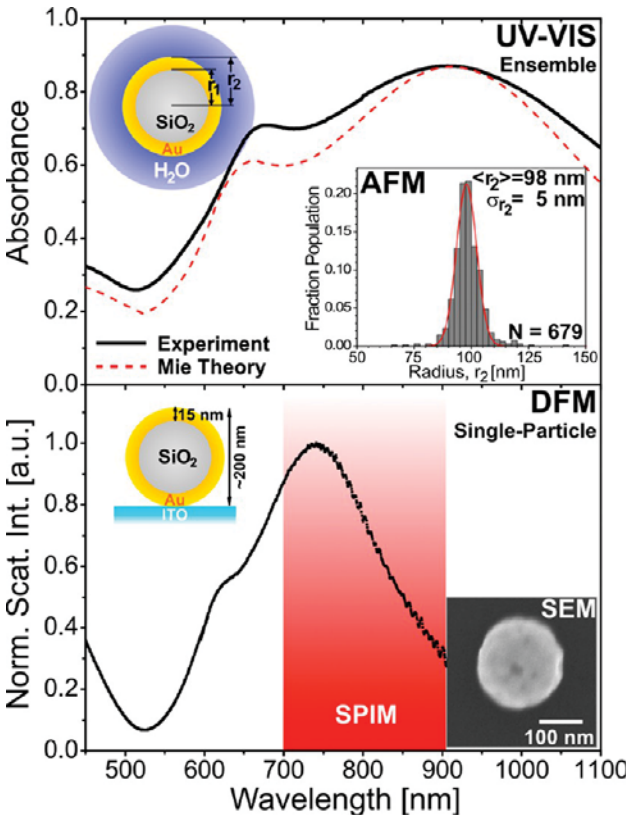

Figure 1. (a) Experimental (black solid line) and Mie simulated (red dashed line) UV−vis spectrum of the aqueous solution of Au nanoshells, with inner and outer radii dimensions $[r_1, r_2]$ = [83, 98] nm and σ_{r_2} = 5 nm. Inset shows the height distribution of Au nanoshells determined in an AFM. (b) Dark-field scattering spectrum of a single Au nanoshell deposited on an ITO-coated glass coverslip. The SEM image of the same particle is shown in the inset. Note the dramatic blue-shift in plasmon resonance upon transfer from aqueous environment onto the ITO substrate.

quadrupolar and dipolar LSP resonance are apparent at $\lambda \sim 660$ nm and λ = 906 nm, respectively, with the corresponding full-width-half-maximum (fwhm) widths of $\Delta\lambda_{fwhm} \sim 90$ nm and $\Delta\lambda_{fwhm} \sim 600$ nm. Strong sensitivity of the dipolar LSPR on shell structural parameters is exploited to infer the ensemble-averaged shell inner and outer radius $[r_1, r_2]$ = [83, 98] nm through Mie theory fitting of the extinction spectrum [Figure 1 (top); dashed line]. The dimensions are further confirmed by atomic force microscopy (AFM) and scanning electron microscopy (SEM) measurements [see Figure 1 inset]

dx.doi.org/10.1021/jp407424n | J. Phys. Chem. C 2013, 117, 22545−22559

performed on a Digital Instruments 3100 dimensional AFM microscope and FEI 650 ESEM microscope, respectively. The concentration of the Au nanoshell solution is estimated at $C = 4.3 \times 10^9$ NP/mL based on a Beer's Law calculation:[48] $C = 2.303 \times \eta_c \times A_{ext}/(\sigma_{ext} \times b)$, where η_c is the dilution factor ($\eta_c = 3.5$), A_{ext} is the measured absorbance at the dipolar plasmon resonance ($A_{ext} \sim 0.85$), σ_{ext} is the extinction cross section at the peak plasmon resonance simulated by Mie theory ($\sigma_{ext} \sim 1.6 \times 10^{-9}$ cm^2), and b is the optical path length of the cuvette ($b = 1$ cm).

Sample Preparation. A 40 μL aliquot of the Au nanoshell solution ($c \sim 4.3 \times 10^9$ NP/mL) is drop-cast onto an ozone-cleaned, registered ITO-coated glass coverslip.[36] After a 60 s settling period, the sample is spun at 1500 rpm for 5 min to remove any excess solution and dry the coverslip. The sample is then successively dipped for 60 s each in spectroscopic grade water, methanol, and acetone to remove any nonparticulate matter. Afterward, the sample is studied in a dark-field microscope and within a couple of hours loaded into a differentially pumped high-vacuum chamber ($P \sim 5 \times 10^{-7}$ Torr) that contains our scanning photoemission imaging microscope (SPIM). Samples were then studied extensively using polarization-dependent SPIM methods over the course of the next 4 weeks. All *correlated* SEM/DFM/SPIM studies were performed roughly 1 year later, over which aging of the nanoshell surface cannot be ruled out as a possibility. However, no differences in the photoelectron emissivity behavior have been observed after that time period.

Dark-Field Microscopy (DFM). Light-scattering spectra of individual, supported Au nanoshells are measured with a dark-field microscope system (Olympus IX-71) coupled to a spectrometer (Acton SpectraPro 150, 150 g/mm diffraction grating) and an EMCCD camera (Princeton Instruments, Cascade II) operated without multiplication. Unpolarized, white light from a tungsten/halogen lamp and a dark-field condenser with a numerical aperture NA = 0.80−0.92 provide the dark-field illumination. Individual Au nanoshells appear as diffraction-limited bright objects on a dark background with the scattered light collected by a 40X air objective (NA = 0.75) resulting in a typical signal-to-background ratio of S/B ∼ 9. Detailed information on the experimental setup and the acquisition of scattering spectra can be found elsewhere.[36]

The scattering spectrum of a representative Au nanoshell supported on ITO is shown in the bottom panel of Figure 1. The two peaks corresponding to the quadrupolar and dipolar LSP resonance apparent at $\lambda = 615$ nm and $\lambda = 744$ nm, respectively, are blue-shifted from their measured ensemble-averaged values in aqueous solution by $\Delta\lambda \sim 45$ nm ($\Delta E \sim 0.15$ eV) and $\Delta\lambda \sim 160$ nm ($\Delta E \sim 0.30$ eV). This shift originates due to the well-known sensitivity of LSP resonances to the refractive index of the local nanoparticle environment.[50−55] In fact, transfer of Au nanoshells from water onto an ITO−air interface is expected to decrease the effective refractive index of the surrounding, thus blue-shifting the LSP resonance into better agreement with observations.[56]

Scanning Photoemission Imaging Microscopy (SPIM). The SPIM technique provides powerful access to multiphoton photoelectron emission from individual metallic (or semiconductor) nanoparticles.[33,34,57] The nonlinear sensitivity of MPPE yield to local electromagnetic fields near the nanoparticle surface allows plasmon-induced near-field enhancement factors to be inferred, as described in greater detail elsewhere.[35,36] Briefly, the fundamental output of a tunable (λ = 710−890 nm; $E_{h\nu}$ = 1.75−1.40 eV) ultrafast Ti:Sapphire laser system operated at 90 MHz is focused by a reflective-type microscope objective (NA = 0.65) to a diffraction-limited spot on an ITO-coated coverslip sample located in vacuum (∼5×10^{-7} Torr). At the focus, the high laser intensity promotes a fraction of electrons within the sample material to the vacuum level, where they are detected by a Channeltron electron multiplier with 45% collection efficiency. In the current study, Fourier-transform limited laser pulses ($\tau_P \sim 50$ fs) with typical pulse energies $E_P = 0.2$ pJ are employed. The resulting modest peak laser intensities of $I = 6 \times 10^8$ W/cm^2 lead to electron ejection via the multiphoton photoelectric effect and typical photoemission rates >10^5 e$^-$/s from individual Au nanoshells, with essentially negligible background signal from the ITO thin film (<0.1 e$^-$/s), as indicated by the SPIM image in Figure 2(a). Correlated SPIM and SEM scans of the same sample area [Figure 2(b)] unambiguously confirm that the observed photoemission signals originate from individual Au nanoshells.

Secondary Electron Microscopy (SEM). SEM images are acquired on an FEI Nova NanoSEM 630 system with a

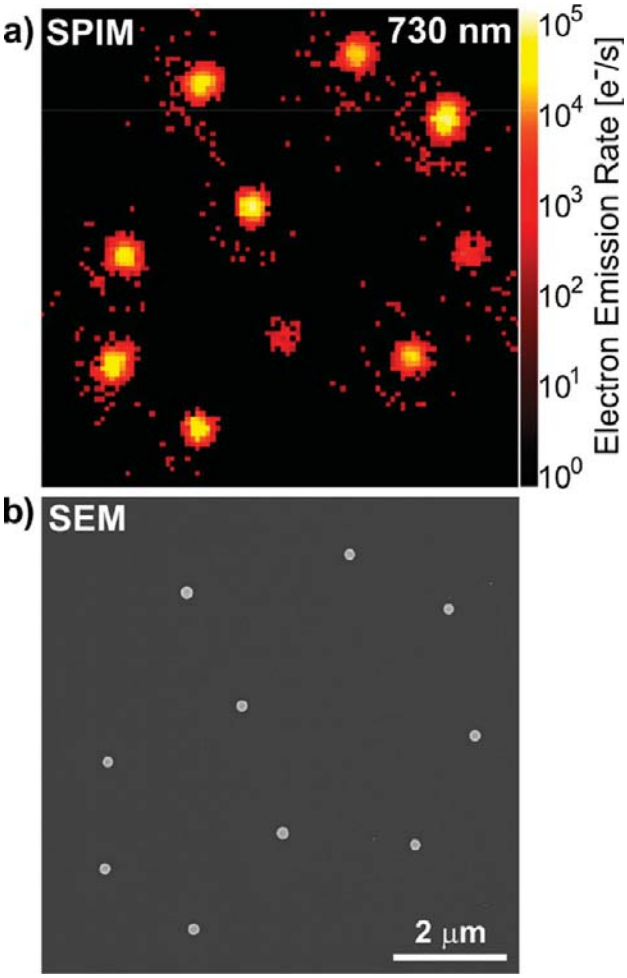

Figure 2. (a) Scanning photoemission imaging microscopy (SPIM) image of individual Au nanoshells on an ITO-coated glass coverslip, recorded with circularly polarized ultrafast laser light at $\lambda = 730$ nm and peak intensity $I = 2.0 \times 10^9$ W/cm^2. Electron emission rate is plotted on a logarithmic scale. (b) Corresponding SEM image of the same sample area indicates that the observed electron emission signal in SPIM images originates from individual Au nanoshells.

dx.doi.org/10.1021/jp407424n | J. Phys. Chem. C 2013, 117, 22545−22559

through-lens detector (TLD) in immersion mode. The front grid of the detector is biased to +150−200 V to improve the collection efficiency of secondary electrons. Typically a 10 kV electron beam at a 1.5 spot size setting is employed, with signals generally integrated for 40 μs. At these conditions, a spatial resolution of ∼3−5 nm and a signal-to-noise ratio S/N ∼ 10 is routinely achieved at >200 000× magnification. The SEM studies are always performed after the SPIM and DFM measurements to avoid any potential sample degradation effects.[58]

Numerical Calculations. A finite-element method (FEM) analysis implemented in COMSOL Multiphysics software package (v4.2) is employed to numerically calculate the near-field distributions and far-field properties (i.e., absorption, scattering, and extinction spectra) of the Au nanoshells, as previously described in greater detail.[59] A concentric arrangement of the Au shell around a SiO_2 core is assumed, with dimensions chosen to conform to the experimentally determined inner and outer shell radii (r_1 = 83 nm and r_2 = 98 nm, respectively). Since we are mainly interested in how various nanoscale structural features on the surface of Au nanoshells affect the electromagnetic near-field enhancements, all calculations are performed with Au nanoshells in vacuum (n = 1). Bulk dielectric properties are presumed for all materials involved, with wavelength-dependent real and imaginary parts of the refractive index [$n(\lambda)$ and $k(\lambda)$, respectively] for Au obtained from the literature.[60] Wavelength-independent refractive index values are assumed for SiO_2 (n = 1.45, k = 0).

III. RESULTS

In the multiphoton photoelectric effect, the photoemission rate N_{PE} scales with the excitation laser intensity I according to the following expression

$$N_{PE} = \sigma_{PE}^{(n)} I^n \quad (1)$$

In eq 1, n is the minimum number of photons required to promote an electron from the conduction band to the vacuum level, and $\sigma_{PE}^{(n)}$ is the n-photon photoemission cross section. Linear trends observed in log−log plots of N_{PE} vs laser intensity [Figure 3(a)] for a representative Au nanoshell on ITO (red squares) clearly indicate the multiphoton photoelectric origin of the detected electrons, at least for laser intensities up to $I = 5 \times 10^8$ W/cm^2. The least-squares measured slope of the line fit [n = 4.1(1)] implies that photoemission from Au nanoshells at λ = 770 nm ($E_{h\nu}$ = 1.61 eV) is a four-photon process, consistent with expectations given the typical work function of gold (Φ_{Au} ∼ 5.0 eV). These findings are confirmed on a total of N = 29 nanoshells, which yield an ensemble-averaged value of $\langle n \rangle$ = 3.7(1) [see inset to Figure 3(a)].

The observed photoemission signal from individual Au nanoshells is remarkably strong and is measured to be ∼10^8-fold greater than the background from the ITO substrate [see Figure 3(a); black squares]. In fact, the studied Au nanoshells exhibit some of the highest photoemissivities observed among various plasmonic nanoparticle systems.[35,36] This is especially surprising because the predicted electromagnetic near-field enhancement at the surface of a perfect Au nanoshell is predicted to be relatively low [i.e., $(|\mathbf{E}|/|\mathbf{E_0}|)_{MAX}$ ∼ 6] and only weakly affected by the experimentally observed heterogeneity in particle size and shell thickness. Moreover, the electromagnetic near-field enhancement factor is lower than those found around other previously studied nanoparticle structures, such as Ag

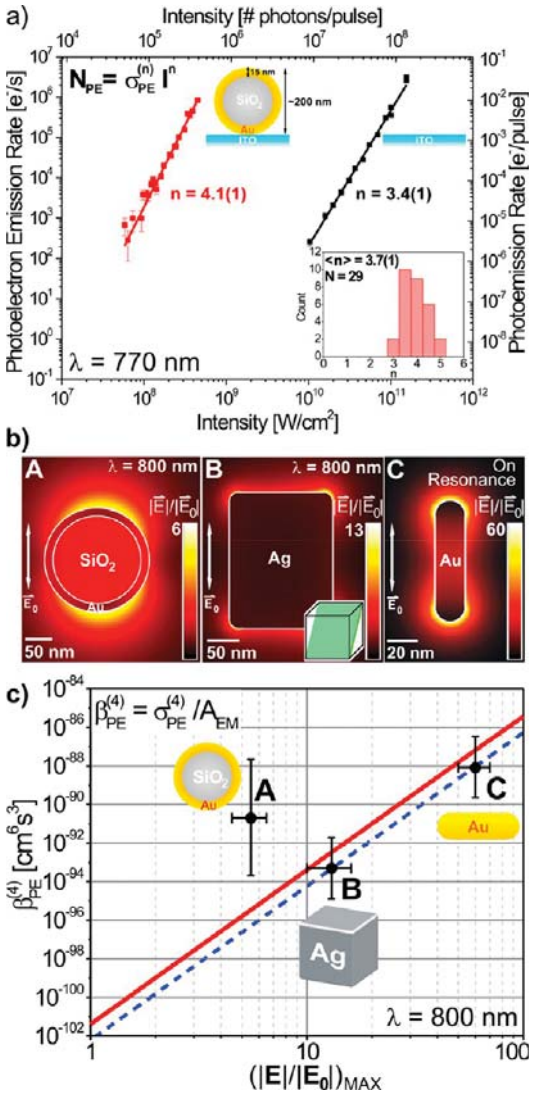

Figure 3. (a) Log−log plot of measured electron emission rate as a function of laser intensity (circularly polarized, λ = 770 nm) for a representative Au nanoshell (red) on an ITO substrate (black). Fits (solid lines) indicate electron emission is a four- and three-photon process for Au nanoshells and ITO, respectively. Inset shows a histogram of the fitted n values for N = 29 Au nanoshells. (b) Numerically calculated electric field enhancements for: (A) Au nanoshell [r_1, r_2] = [83, 98] nm at λ = 800 nm; (B) Ag nanocube (edge length, d = 160 nm; corner radius, r = 16 nm) at λ = 800 nm; and (C) Au nanorod (length, L = 80 nm; width, W = 20 nm) on resonance at λ = 680 nm. All calculations are performed for particles in vacuum with vertically polarized light propagating to the right. (c) Four-photon photoelectron emissivity $\beta_{PE}^{(4)}$ of the three nanoparticle systems as a function of the maximum electric field enhancement $(|\mathbf{E}|/|\mathbf{E_0}|)_{MAX}$ for λ = 800 nm excitation. Predictions of a coherent multiphoton photoelectron emission model by Yalunin et al. (ref 63) for electron emission from a free-electron metal (Φ = 4.8 eV, E_F = 5.5 eV) are also shown (red solid line). Nanocubes and nanorods (B and C) agree well with the predictions, whereas Au nanoshells (A) are significantly more photoemissive than expected. The vertical error bars indicate the typical range of emissivities observed for different particles of the same geometry. Dashed line represents a best-fit to the crystalline nanocube and nanorod samples, based on a $(|\mathbf{E}|/|\mathbf{E_0}|)^8$ dependence expected for four-photon photoemission.

dx.doi.org/10.1021/jp407424n | J. Phys. Chem. C 2013, 117, 22545−22559

nanocubes and Au nanorods [see Figure 3(b)]. Since $\sigma_{PE}^{(n)}$ scales rapidly with $(|\mathbf{E}|/|\mathbf{E}_0|)_{MAX}^{2n}$,[35,36,61,62] one might anticipate Au nanoshells to be relatively weak photoelectron emitters, even after taking into account their relatively large emitter area compared to the other two nanoparticle systems.

Instead, unexpectedly high photoemissivities are observed for Au nanoshells as showcased in Figure 3(c), where we plot the four-photon photoemission cross section $\beta_{PE}^{(4)} = \sigma_{PE}^{(4)}/A_{EM}$ normalized to the COMSOL inferred emitter area (A_{EM}) for three different nanoparticle systems [see Figure 3(c)] as a function of the maximum electromagnetic near-field enhancement factor $(|\mathbf{E}|/|\mathbf{E}_0|)_{MAX}$ around the nanoparticles. It is important to note that the photoemissivity values for Ag nanocubes and Au nanorods agree relatively well with the theoretical predictions of a coherent multiphoton photoelectron emission model by Yalunin et al. for solids[63] but adapted for plasmonic nanostructures (solid line).[36] To account for plasmon-induced near-field effects, the theoretically predicted photoemission values for the bulk ($\beta_{PE}^{(4)}$) are simply scaled by the maximum local electromagnetic field enhancement raised to the appropriate power, i.e., $(|\mathbf{E}|/|\mathbf{E}_0|)_{MAX}^{8}$. Good agreement between theory and experiment is obtained for Ag nanocubes and Au nanorods and likely arises due to the crystalline nature of the two nanoparticle systems. In other words, because both nanorods and nanocubes are highly crystalline, the near-field distributions calculated for their idealized geometries [see Figure 3(b); B, C] are expected to accurately predict the experimentally attainable near-field enhancements in both structures.

In contrast, the measured $\beta_{PE}^{(4)}$ values for Au nanoshells based on the near-field distributions calculated around its idealized structure [see Figure 3(b); A] deviate markedly ($\sim 10^5$-fold too high) from the experimental trends set by the other two particle systems (dashed line), as well as from theoretical predictions (solid line). This finding suggests that significantly higher near-field enhancement regions $[(|\mathbf{E}|/|\mathbf{E}_0|)_{MAX} \sim 20]$ exist on the surfaces of Au nanoshells than expected from the smooth model shape depicted in Figure 3(b), A. It is important to note that these $\beta_{PE}^{(4)}$ values assume that the surface of an entire Au nanoshell (radius, $r \sim 100$ nm) serves as the emitter area. Since the actual photoemitting region (i.e., the hot spot) likely represents only a fraction of this total surface area, much larger enhancement factors of $(|\mathbf{E}|/|\mathbf{E}_0|)_{MAX} \sim 40$ or even $(|\mathbf{E}|/|\mathbf{E}_0|)_{MAX} \sim 60$ would be inferred for photoemission from a more localized surface morphology with a scale size of $r \sim 10$ nm or $r \sim 1$ nm, respectively.

Another experimental observation that contrasts Au nanoshell behavior with their more crystalline counterparts (i.e., Au nanorods and Ag nanocubes) is the remarkable dynamic range and degree of inhomogeneity observed in the overall photoemission intensity. For example, strongly photoemitting Au nanoshells may emit as much as 10^6-fold more intensely than weakly emitting ones at the same laser excitation conditions. By way of contrast, Au nanorods and Ag nanocubes exhibit a considerably narrower spread in $\beta_{PE}^{(4)}$ values ($\sim 10^2$-fold), as indicated by their smaller vertical "error" bar in Figure 3(c). It is important to note that due to the eighth power scaling of the experimental signals with $|\mathbf{E}|/|\mathbf{E}_0|$ our photoemission model can readily account for the observed dramatic particle-to-particle variations by relatively modest changes in the near-field enhancement. Nevertheless, this million-fold dynamic range suggests a sizable spread in near-field enhancement values $(\sim(10^6)^{1/8} \sim 5)$ between different Au nanoshell particles and quite possibly also a significant variation in the contributing hot spot morphologies.

Critical supporting evidence that one or at most a few localized hot spots rather than uniform surface emission are responsible for the strong multiphoton photoemissivity of Au nanoshells can be obtained from measurements of the photoemission current as a function of excitation laser polarization. On the basis of spherical symmetry [see Figure 3(b), A], the dependence of photoelectron yield on laser polarization should be completely isotropic for an idealized Au nanoshell. In stark contrast, a strong dependence of electron emission current on polarization direction θ is observed [see Figure 4(a)]. The observed behavior is well described by a

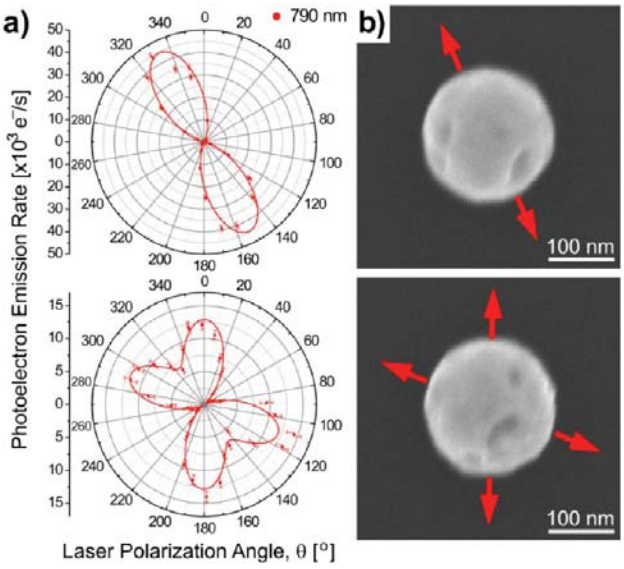

Figure 4. (a) Photoelectron emission rate from two representative Au nanoshells as a function of laser polarization angle, θ, at $\lambda = 790$ nm ($I = 8 \times 10^8$ W/cm^2). (b) SEM images of the corresponding Au nanoshells in the same reference frame. Arrows indicate laser polarization directions that generate maximum electron emission.

$\cos^8(\theta)$ function, consistent with four-photon photoemission from a *single* hot spot on the nanoshell surface. While most studied Au nanoshells exhibit this single hot spot polarization behavior, nanoshells are occasionally (<10%) probed that exhibit four-lobed polar plot patterns, consistent with the relatively rare occurrence of *two* strongly near-field enhancing hot spots [see Figure 4(a), bottom].

To identify the geometry of the observed hot spots, we correlate photoemission polar plots with SEM images of the Au nanoshells, as shown for two representative cases in Figure 4. The surface of a typical Au nanoshell can be seen to be decorated with a myriad of asperities and pinhole-like defects ranging from 10 to 50 nm in size. Yet, only one or two highly photoemissive regions are typically identified in SPIM, indicating that only a subpopulation of these defects is responsible for the inferred high near-field enhancement. From a systematic study of many such SEM images, we find that the excitation polarization directions resulting in the strongest photoemission are often aligned with edges of pinhole-like defects (shaded areas). However, comparably many counterexamples are also found where strong photoemission enhancement with laser polarization alignment is completely uncorrelated with any visible defects. This implies

dx.doi.org/10.1021/jp407424n | J. Phys. Chem. C 2013, 117, 22545−22559

morphologies smaller than the resolution of our SEM (3−5 nm) are quite possibly responsible for the strongest near-field enhancements, suggesting $(|\mathbf{E}|/|\mathbf{E}_0|)_{MAX} \sim 50$ or greater may exist near such features.

The near-field origin of photoelectron emission and the importance of hot spots in photoemission from Au nanoshells are further demonstrated through correlated dark-field microscopy (DFM) and SPIM measurements. In Figure 5(a), the photoemission rate as a function of excitation wavelength for three representative Au nanoshells (red) is compared with their corresponding light scattering spectra (black). The far-field signature of the dipolar LSP resonance can be clearly observed in light scattering at $\lambda \sim 740$ nm. The resonant wavelength exhibits only minor particle-to-particle variations as evidenced by the narrow distribution of LSP resonances in the studied sample of Au nanoshells on ITO, shown in Figure 5(b). The ensemble average $\langle\lambda_{PI}\rangle = 736(1)$ nm and fwhm = 36(2) nm have been determined for a representative sample of $N = 146$ nanoshells [Figure 5(b) top]. This result indicates a relative homogeneity of the sample in terms of global structural parameters such as particle size and shell thickness, which, for this nanoparticle system, predominantly determine the resonance frequency of the dipolar plasmon in the *far field*.

On the other hand, a significantly more pronounced heterogeneity is observed in the *near-field* properties of Au nanoshells, as evidenced by approximately 3-fold [fwhm = 115(20) nm] broader *ensemble distribution* of photoemission resonances [see Figure 5(b) right]. Additionally, the large spread in a plot correlating photoemission with scattering resonances [Figure 5(b) center] indicates that the two types of resonances appear *uncorrelated* in the studied Au nanoshell samples. A similar behavior has been observed previously in Au nanostars by Hrelescu et al., where nanoscale morphology of the tips was seen affecting photoemission (*near-field* phenomenon) significantly more than light scattering (*far-field* phenomenon).[44] However, both these cases contrast with Au nanorods, where a strong correlation between near- and far-field resonances has been clearly demonstrated, presumably due to the well-defined crystalline structure of this nanoparticle system.[36] Our current findings thus not only confirm the near-field origin of photoemission from Au nanoshells but also indicate the existence of various hot spot morphologies on the nanoshell surfaces that lead to a different spectral dependence of the nanoparticle near-field enhancement factors.

Another interesting observation is that the photoemission resonances of Au nanoshells appear to be narrower than their corresponding scattering resonances. For example, plasmon resonance widths inferred from scattering spectra (Figure 6 top) reveal an ensemble-averaged mean $\langle\Delta\nu_{PI}\rangle = 0.391(3)$ eV ($N = 146$), implying a plasmon dephasing time $T_2 = 2\hbar/\Delta\nu_{PI} \sim 3$ fs, consistent with observations on similarly sized Au nanospheres.[64] On the other hand, a 2-fold smaller ensemble-averaged value is determined for photoemission, i.e., $\langle\Delta\nu_{SPIM}\rangle = 0.186(2)$ eV (Figure 6 right). This can be understood in terms of the nonlinear nature of the photoemission process, in which the signal dependence on $(|\mathbf{E}|/|\mathbf{E}_0|)^8$ tends to narrow resonances observed in linear processes such as light scattering, where signal scales roughly with $(|\mathbf{E}|/|\mathbf{E}_0|)^2$. Specifically, if one assumes a Gaussian spectral line shape for $(|\mathbf{E}|/|\mathbf{E}_0|)^2$, then the four-photon photoemission resonance width would be expected to simply follow $\Delta\nu_{SPIM} = \Delta\nu_{LSPR}/\sqrt{4}$, where $\Delta\nu_{LSPR}$ is the scattering resonance width. Such a trendline is plotted in Figure 6 (dashed line), which indicates a strong 1:2 correlation between $\Delta\nu_{SPIM}$ and the corresponding $\Delta\nu_{LSPR}$. Note that all studied Au nanoshells fall either on or below this trendline,

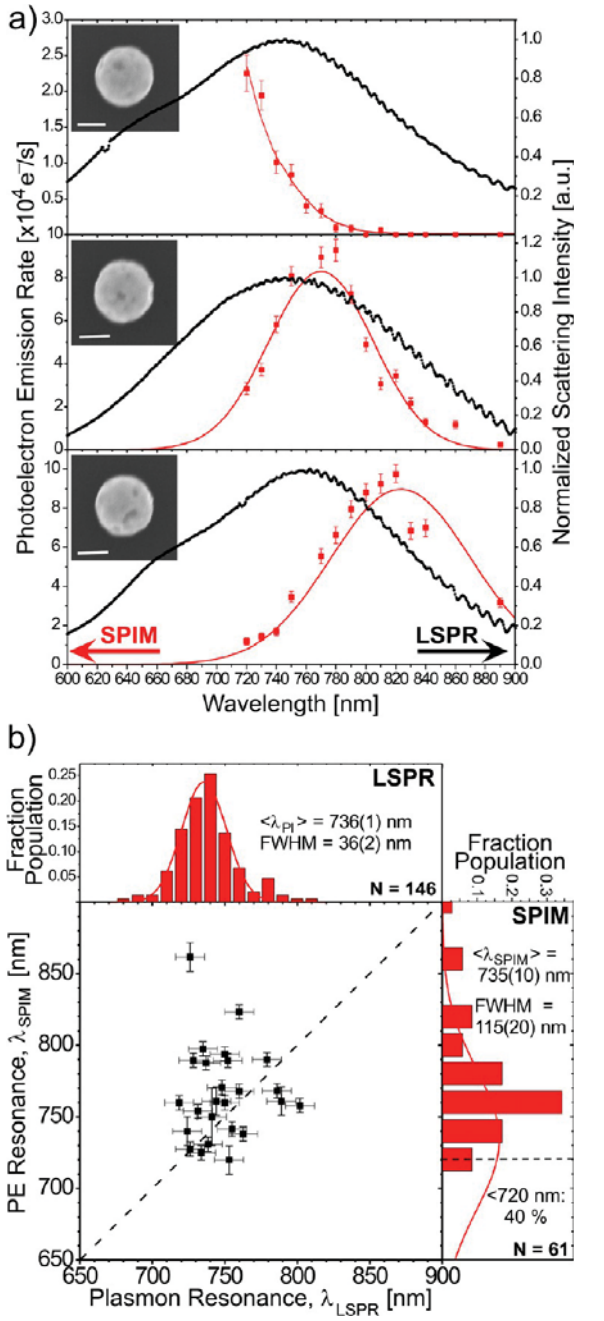

Figure 5. (a) Correlated dark-field scattering (black) and photoemission (red) spectra of three representative Au nanoshells. Photoemission and scattering resonance peaks do not appear correlated. Insets show SEM images of the corresponding Au nanoshells. Scale bar is 100 nm. (b) Photoemission resonances, λ_{SPIM}, as a function of scattering resonances, λ_{LSPR}, for $N = 25$ Au nanoshells. Dashed line marks perfect correlation between the two quantities, whereas the large scatter observed indicates that λ_{LSPR} and λ_{SPIM} are uncorrelated. Adjoining histograms depict the ensemble distribution of scattering (top) and photoemission resonance peaks (right) in the sample. A relatively tight distribution of dipolar resonances are observed, whereas photoemission resonance peaks are distributed over a much broader wavelength range with almost half of them exhibiting only tails on the blue end of the tuning range.

dx.doi.org/10.1021/jp407424n | J. Phys. Chem. C 2013, 117, 22545−22559

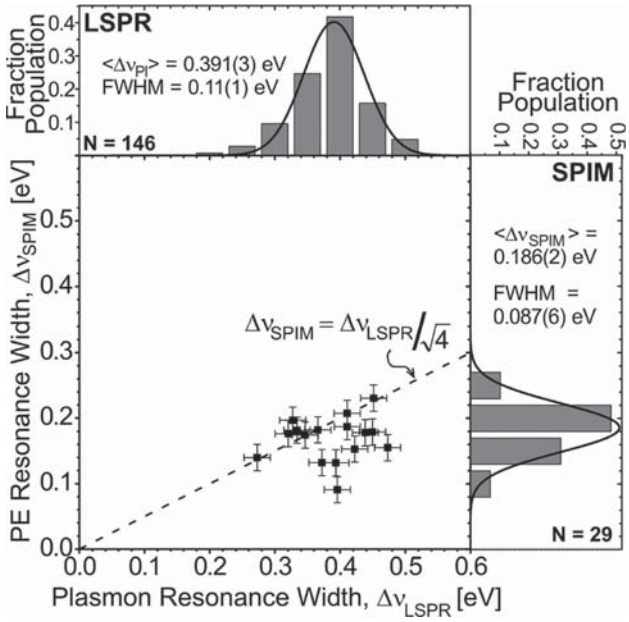

Figure 6. Correlation plot between widths of light-scattering resonances $\Delta\nu_{LSPR}$ and photoemission resonances $\Delta\nu_{SPIM}$. Photoemission (PE) resonances are typically 2-fold narrower than the corresponding light-scattering resonances, in agreement with the expected $\sqrt{n}$-fold plasmon resonance narrowing due to the nonlinearity of the n-photon (n = 4) photoemission process (dashed line). The ensemble distribution of light scattering and photoemission resonance widths in the Au nanoshell sample is shown in the histogram on the top and right, respectively, along with the Gaussian best-fit lines.

suggesting not only that the upper limit on photoemission resonance width is determined by the underlying plasmon lifetime but also that about a half of the nanoshell population meets this intrinsic limit. The other half displays tighter photoemission resonances, indicating the presence of hot spots that exhibit as much as 2-fold narrower wavelength-dependent $(|\mathbf{E}|/|\mathbf{E}_0|)^2_{MAX}$ factors than expected based on the far-field (i.e., light scattering) resonance width and thus the plasmon lifetime.

A further indication that the wider photoemission resonances may be inhomogeneously broadened even on a single-particle basis stems from the measured wavelength sensitivity of the polarization-dependent photoemission patterns, as shown for two representative Au nanoshells in Figure 7. In Figure 7(a), the photoemission spectrum recorded with circularly polarized excitation reveals that photoelectron current in this nanoshell peaks for $\lambda \sim 790$ nm, with the observed signal predominantly arising from a hot spot oriented along $\theta \sim 155°$. As one tunes spectrally away from the main resonance, the photoemission rate decreases, but more importantly, the photoelectron emission pattern itself changes. For example, excitation with $\lambda \sim 730$ nm reveals that the photoemission is dominated by a different hot spot, which is aligned along $\theta \sim 135°$.

This behavior is even more apparent in the case of the second Au nanoshell [Figure 7(b)], where two hot spots are found contributing to the observed photoemission rate at λ = 790 nm, with each carrying approximately equal weight. The feature aligned with $\theta \sim 0°$ appears to peak at $\lambda \sim 790$ nm, whereas the one oriented along $\theta \sim 120°$ reaches a maximum nearer the red end of the studied spectral range. In fact, the Gaussian fit quality of the photoemission spectrum in Figure

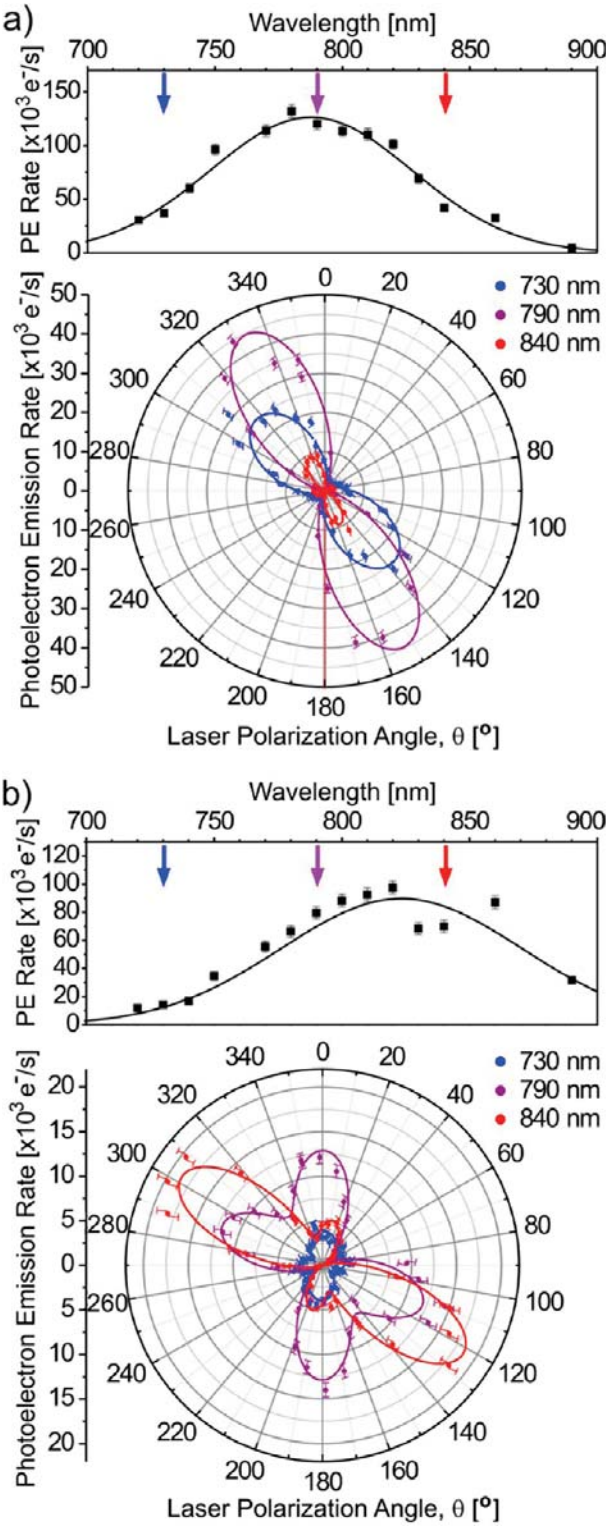

Figure 7. (a,b) Excitation wavelength (top) and polarization (bottom) dependence of the photoelectron emission rate from two representative Au nanoshells. Relatively broad resonances are observed in the photoemission spectra. Changing patterns in the polar plots acquired for three different excitation wavelengths suggest electric near-field enhancement of different hot spots exhibits different wavelength dependence.

dx.doi.org/10.1021/jp407424n | J. Phys. Chem. C 2013, 117, 22545−22559

7(b) is limited by the presence of two hot spots that result in a similar near-field enhancement factor at two well-separated wavelengths (i.e., $\lambda \sim 790$ and $\lambda \sim 850$ nm). This more complex behavior suggests that multiple hot spots may exist on the nanoshell surface, with each one giving rise to near-field enhancements that differ in both magnitude and wavelength dependence.

An intriguing "seasoning" phenomenon is observed in photoemission from Au nanoshells, whereby the photoelectron signal can undergo a dramatic 10- to 100-fold *increase* upon prolonged illumination, even at relatively low peak laser intensities ($<4 \times 10^8$ W/cm^2). This is demonstrated in Figure 8 by a sequence of consecutively acquired SPIM images for

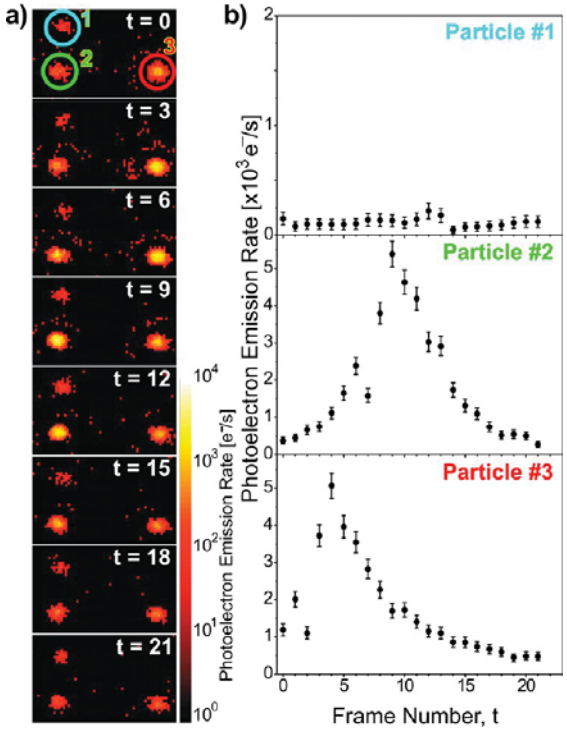

Figure 8. (a) Sequence of images of a fixed sample area recorded sequentially that indicate the time dependence of the photoemission signal. Images are recorded using circularly polarized light with $\lambda = 730$ nm and $I = 1.4 \times 10^8$ W/cm^2, where the average illumination time of a particle per frame is $\Delta t \sim 4.4$ s (i.e., 4×10^8 pulses). The signal from the three nanoshells is graphed as a function of frame number t in (b). At the utilized intensity levels, a temperature increase of $\Delta T \sim 1$ K is anticipated, suggesting thermal evaporation of either the ligand layer or Au metal is unlikely.

three Au nanoshells on ITO and by the associated "time" traces of the particle peak photoemission rate within each frame. The photoelectron current from two nanoshells is observed to increase 10-fold during the scan sequence recorded at $I = 1.4 \times 10^8$ W/cm^2 and $\lambda = 730$ nm. Almost all Au nanoshells are found to exhibit this "spiking" photoemission behavior in the laser intensity range $I = (1 - 4) \times 10^8$ W/cm^2, after which they settle down to a substantially more constant level.

Due to this additional dynamic variability of the nanoparticles, we focus our collection of photoemission data on the "post-spiking" regime, once the nanoshell signal has stabilized. To ensure that this transient behavior incurs no qualitative change on the spatial distribution of hot spots on individual Au nanoshells, laser polarization photoemission patterns are recorded as a function of time for the particle photoemissivity (Figure 9). The polar plots, shown in Figure 9(b), are acquired

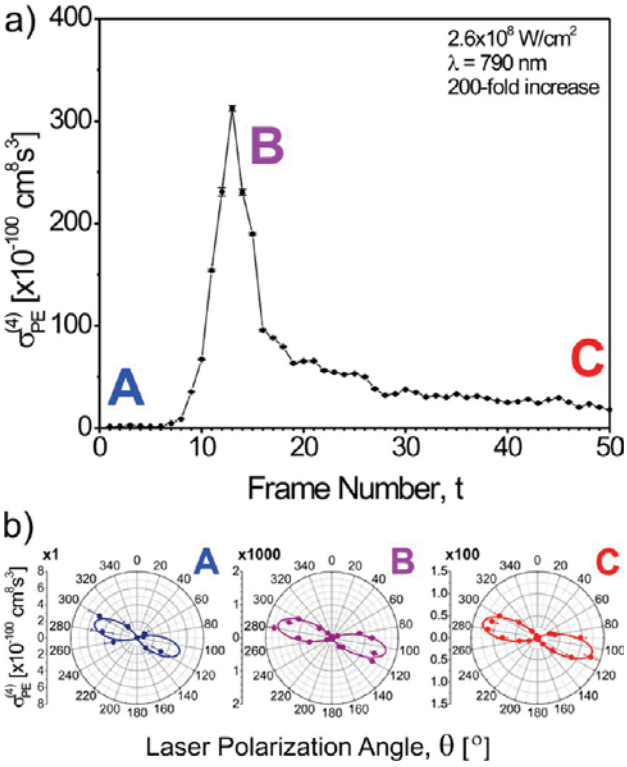

Figure 9. (a) Time-dependent photoelectron emission signal from a representative Au nanoshell recorded with circularly polarized light of intensity $I = 2.6 \times 10^8$ W/cm^2. (b) At indicated points, A–C, in (a) the electron emission as a function of the linear laser polarization is recorded for $\lambda = 790$ nm. No change in the polarization-dependent electron emission patterns is observed during the transition that dramatically increases the overall photoelectron yield.

prior to (A), on (B), and post (C) photoemission spike at low enough laser intensities for the photoelectron signal to remain stable during a laser polarization scan. In all three cases, identical photoemission patterns are observed, indicating a persistent hot spot distribution on nanoparticles regardless of particle photoemissivity. These plots suggest that the process leading to a sudden jump in photoelectron yield leaves the hot spot(s) largely intact. This effect could be attributable to the presence of impurities in individual hot spots.

It is worth noting that changes in the hot spot distribution can be induced at elevated laser intensities, suggestive of structural rearrangement in the Au layer. For example, 10-fold higher laser intensities ($I \sim 5 \times 10^9$ W/cm^2) can cause the photoemission from a specific hot spot structural feature to diminish. This is nicely demonstrated in Figure 10(a) by a vastly reduced lobe (red) in the "burn-in" direction at $\theta = 20°$. Note that the nearly orthogonally oriented lobe (blue) at $\theta = 100°$ maintains photoemission levels, indicating negligible change in its underlying hot spot morphology. Interestingly, a new lobe (purple) appears along $\theta = 140°$, which was absent prior to the "burn-in" process of the nanoshell in Figure 10(a). This is even more apparent in Figure 10(b), where a previously buried lobe along $\theta = 100°$ gains more than an order of magnitude in photoemissivity and begins to completely

dx.doi.org/10.1021/jp407424n | J. Phys. Chem. C 2013, 117, 22545–22559

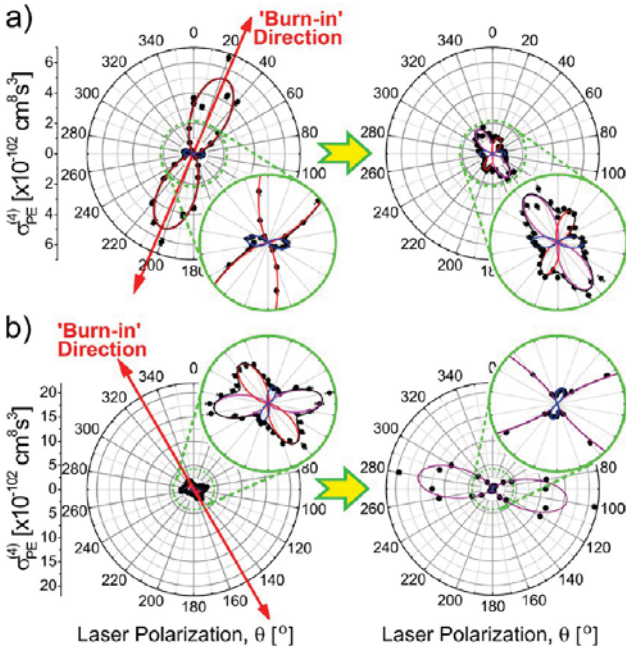

Figure 10. Multiphoton photoelectron emission as a function of laser polarization for two representative Au nanoshells before (left) and after (right) irradiation with linearly polarized laser light oriented along the indicated, "burn-in", direction (red arrow) for a total of ~1 s. The polarization dependence as well as the burn-in is accomplished using λ = 790 nm laser light of intensity (a) $I = 6.9 \times 10^9$ W/cm^2 and (b) $I = 1.2 \times 10^{10}$ W/cm^2. At these conditions the polarization patterns can be modified, suggesting a structural rearrangement of the Au nanoshell itself.

dominate the photoemission pattern. This behavior is reminiscent of the spike in photoelectron rate observed with circularly polarized light of lower intensity (see Figures 8 and 9), except that linear polarization selectively induces this transition among the aligned subset of hot spots. Consistent with this picture, the weak lobe (blue) in near normal orientation with respect to the "burn-in" direction again remains unaffected by the process [see Figure 10(b)].

This strongly polarization-sensitive behavior is a tell-tale sign that *non*thermal process(es) must be impacting the measured changes in photoemissivity. The asperities and crevices typically present on the shell surface do not significantly alter the particle absorption cross section, which remains nearly identical to that of a perfect nanoshell. As a result, the nanoparticle absorbs light equally and thus reaches the same temperature, regardless of the laser polarization direction. Therefore, any thermally driven rearrangement on the shell surface would occur with the laser polarization oriented along any arbitrary direction, in contrast with experimental observations.

To confirm low heat deposition into Au nanoshells at typically employed excitation conditions in SPIM experiments, we perform a simple back-of-the-envelope calculation to estimate the particle temperature increase. On the basis of the assumption that the particle completely cools down by the arrival of the next pulse ~10 ns later, the particle temperature increase ΔT in the absence of a fast cooling process is obtained from

$$\Delta T = \frac{\sigma_{ABS} \cdot I \cdot \tau_P}{C_{NP}} \quad (2)$$

Here, τ_P is the laser pulse duration ($\tau_P \sim 50$ fs); σ_{ABS} is the particle absorption cross section ($\sigma_{ABS} \sim 3 \times 10^{-10}$ cm^2 from COMSOL); and C_{NP} is the nanoparticle heat capacity. To estimate the maximum temperature increase (ΔT_{MAX}) during one cycle, we assume that only the Au shell contributes to C_{NP} due to the high thermal conductivity of Au. Thus, one obtains the expression $C_{NP} = \rho_{Au} \cdot c_{Au} \cdot \pi \cdot (D^3 - d^3)/6$, where the density and specific heat of Au are $\rho_{Au} = 19.3$ g/cm^3 and $c_{Au} = 0.129$ J/g·K, respectively. For a representative Au nanoshell with inner and outer shell radii of $[r_1, r_2] = [83, 98]$ nm, $\Delta T_{MAX} \sim 20$ K at $I = 5.0 \times 10^9$ W/cm^2, implying quite minimal thermal effects.

The validity of this simple model in describing experimental conditions is demonstrated in Figure 11, where signs of

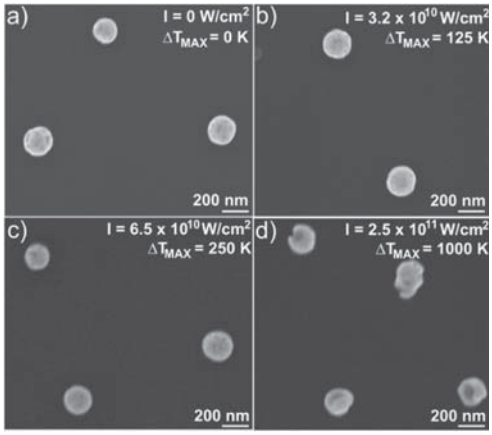

Figure 11. SEM images of Au nanoshells irradiated with ultrafast ($\tau_P \sim$ 50 fs) laser radiation of λ = 730 nm at the indicated intensity levels for ~0.1 s (9×10^6 pulses). No observable structural changes to the particles are observed until $I = 2.5 \times 10^{11}$ W/cm^2, when an estimated temperature increase of ~1000 K suggests the onset of melting.

nanoshell melting are not observed until the predicted $\Delta T_{MAX} \sim 1000$ K [Figure 11(d)], which is consistent with the melting point of Au ($T_M = 1337$ K). It is worth stressing that such melting occurs only at a 1000-fold higher laser intensity (i.e., $I = 2.5 \times 10^{11}$ W/cm^2) than typically employed in the current photoemission measurements. Indeed, even at $I \sim 5 \times 10^{10}$ W/cm^2, where $\Delta T_{MAX} \sim 200$ K is predicted, we see no signs of shell melting in the SEM images [Figure 11(b,c)]. The observations further support the validity of the underlying assumption that the thermal contact between the ITO substrate and the Au nanoshells is sufficient for the nanoparticles to completely cool within the 10 ns time window between adjacent laser pulses.

IV. DISCUSSION

The surprisingly intense multiphoton photoemission from Au nanoshells combined with their strong laser polarization-dependent photoemissivity has been interpreted to originate from enhanced electromagnetic near fields surrounding nanoscale structural features on the shell surface, i.e., hot spots. To demonstrate the dramatic impact small surface features can have on near-field phenomena, COMSOL simulations of near- and far-field properties are performed for a Au nanoshell with a single spherical asperity on its surface. The results for a SiO_2 core−Au shell nanoparticle of representative geometrical dimensions $[r_1, r_2] = [83, 98]$ nm are shown in Figure 12, both for an idealized structure and for one with a spherical

dx.doi.org/10.1021/jp407424n | J. Phys. Chem. C 2013, 117, 22545−22559

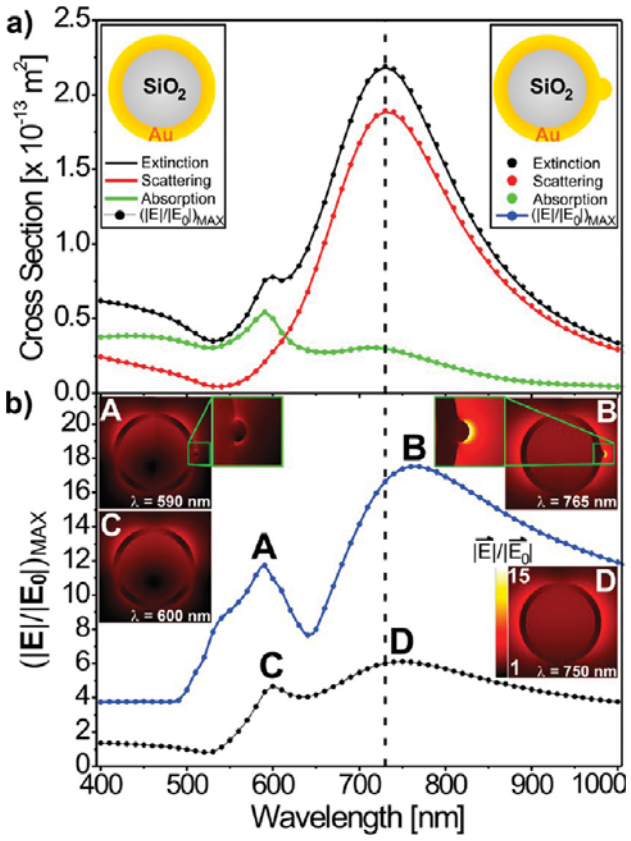

Figure 12. (a) Numerically simulated absorption (green), scattering (red), and extinction (black) spectra of a perfect Au nanoshell (lines) and a Au nanoshell with a small asperity (asperity radius, r_A = 4 nm) on the surface (circles). Few differences in the predicted far-field properties are observed between the two structures. On the other hand, (b) the maximum electric field enhancement near the particle surface $(|\mathbf{E}|/|\mathbf{E_0}|)_{MAX}$ as a function of wavelength shows dramatic differences between a perfect nanoshell (black) and a nanoshell with an asperity (blue). Insets indicate the near-field distribution of electric fields at the specified excitation wavelength for both an imperfect (A, B) and a perfect (C, D) nanoshell.

asperity of radius r_A = 4 nm. Overlapping absorption, scattering, and thus extinction spectra for the two particle shapes, shown in Figure 12(a), confirm our earlier suggestion that small features have little impact on the *far-field* properties of the nanoparticle.

On the other hand, dramatic changes in the *near-field* properties can be induced in the presence of slight surface imperfections, as indicated in Figure 12(b). The addition of this asperity to a perfect Au nanoshell causes a nearly 3-fold increase in $|\mathbf{E}|/|\mathbf{E_0}|$, resulting in $(|\mathbf{E}|/|\mathbf{E_0}|)_{MAX} \sim 18$ at the dipolar LSP resonance ($\lambda \sim 765$ nm). Note that the $|\mathbf{E}|/|\mathbf{E_0}|$ increase occurs throughout the spectrum, indicating that the near-field properties of the nanoparticle can be entirely dominated by such a small feature. For example, most pronounced near-field enhancements are observed around the asperity [A, C in Figure 12(b)] even at the quadrupolar resonance ($\lambda \sim 600$ nm), where the structural feature lies in the nodal plane of the plasmon mode. Due to the $(|\mathbf{E}|/|\mathbf{E_0}|)^8$ sensitivity of the four-photon photoemission cross section, any small asperity-induced increase in near-field enhancement around a nanostructure will strongly amplify the multiphoton photoemission efficiency. Thus, the likely presence of asperities as model hot spot geometries provides a good qualitative explanation of our experimental observations.

With COMSOL simulations we can also explore whether such a model can quantitatively account for the typically measured photoemission rates, specifically, a 10^5-fold higher photoemission cross-section $\sigma_{PE}^{(4)}$ than predicted for a perfect Au nanoshell (see Figure 3). To make this comparison, we integrate the calculated electric near-field enhancement $|\mathbf{E}|/|\mathbf{E_0}|$ raised to the appropriate eighth power over the nanoparticle surface area (A_{NP}), i.e.

$$\sigma_{PE}^{(4)} \propto \int_{A_{NP}} dA \cdot (|E|/|E_0|)^8 \tag{3}$$

From eq 3, it is clear that the four-photon cross-section integral weighs $|\mathbf{E}|/|\mathbf{E_0}|$ enhancement significantly more than emitter area, indicating that even asperities too small to resolve with high-resolution imaging techniques, such as the SEM imaging used in this study, can still dominate the overall photoemissivity. This provides a plausible explanation for the absence of spatially identifiable hot spots in our SEM images of Au nanoshells.

To examine the effect of a hot spot on a Au nanoshell surface more specifically, we look at a series of simulated defect structures on a nanoshell surface and calculate the relative contribution of each defect geometry to the local field enhancement. First, we consider an asperity modeled as a nanoscopic half-sphere of radius r_A on the surface of a Au nanoshell with outer shell radius R. The effect of this half-sphere asperity radius r_A on the maximum electric near-field enhancements is shown in Figure 13(a) for λ = 800 nm excitation and polarization vector collinear with the particle symmetry axis. The electric near-field enhancement factors increase with decreasing asperity size (black circles), reaching a limiting value of $(|\mathbf{E}|/|\mathbf{E_0}|)_{MAX} \sim 20$ as $r_A \rightarrow 0$. Since the corresponding emitter area concurrently decreases, the photoemissivity is expected to peak for some intermediate value of r_A. Photoemissivity as a function of the scale length ratio r_A/R is shown in Figure 13(a) (red squares) and is obtained from eq 3 for electromagnetic near fields calculated 1 nm away from the particle surface. For Au nanoshells with dimensions consistent with our study ($R \sim 100$ nm), the maximum photoemission results for relatively large spherical asperities ($r_A \sim 30$ nm), which would have been straightforward to identify in SEM. Indeed, the predicted photoemissivity increases only ~50-fold compared to a perfect nanoshell, indicating that such visually abundant hemispherical asperities are not solely responsible for the much larger 10^5-fold enhancements observed.

Second, we consider a "pinhole" defect observed on Au nanoshells previously,[65] which we model as the inner half of a torus with an inside diameter g and a thickness $R - r$. In contrast to hemispherical asperities, the maximum $|\mathbf{E}|/|\mathbf{E_0}|$ enhancements are observed for the polarization vector aligned *perpendicular* to the particle symmetry axis. The near-field enhancements in the gap region for $g \leq 25$ nm are found to be *smaller* than those calculated near a perfect nanoshell [Figure 13(b); black circles], indicating that a pinhole defect will not significantly alter the overall photoemissivity of a Au nanoshell. In fact, pinhole contributions to the photoemission current, estimated from $(|\mathbf{E}|/|\mathbf{E_0}|)_{MAX}$ within the gap and the area of the inner torus half A_{TORUS}^{INNER}, account for less than 10% of the emission predicted for a perfect nanoshell [Figure 13(b); (red squares)]. Thus, we conclude that pinhole defects do not correspond to the highly photoemissive hot spots on Au

dx.doi.org/10.1021/jp407424n | J. Phys. Chem. C 2013, 117, 22545−22559

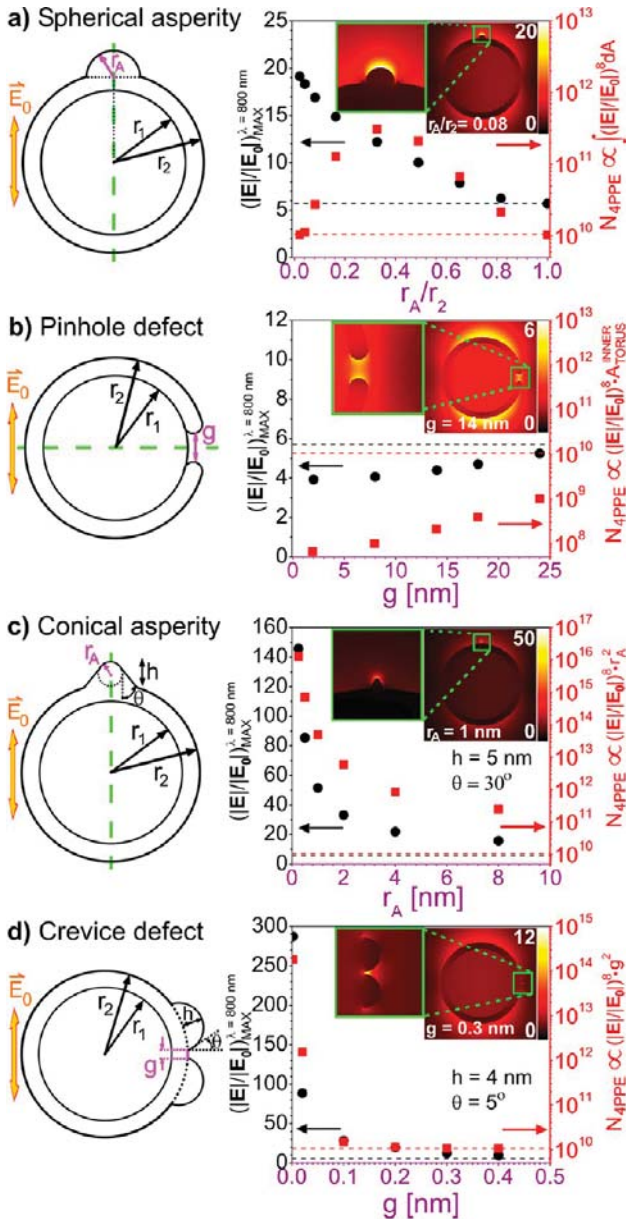

Figure 13. Maximum electric near-field enhancement ($|\mathbf{E}|/|\mathbf{E}_0|$) (black circles) and predicted four-photon photoemissivity N_{4PPE} (red squares) at λ = 800 nm for four different defect types: (a) a spherical asperity with radius r_A, (b) a pinhole with a gap opening g, (c) a conical asperity with a rounded tip of radius r_A, and (d) a crevice defect with an interasperity distance g. Dashed lines indicate the values predicted for a perfect nanoshell with inner and outer radii of r_1 = 83 and r_2 = 98 nm, respectively. Note that sharp features significantly increase the local electric field, suggesting that electron emission from small imperfections on the particle surface may completely dominate the photoelectron emission process. Insets show the distribution of electric fields around a Au nanoshell with a particular surface defect. All studied structures, except (d), are bodies of revolution with the revolution axes marked by dashed green lines.

nanoshells. In fact, any of a number of studied surface *depressions* with a $C_{\infty v}$ symmetry axis have been found to contribute negligibly to the overall photoemissivity, even if they involve a very sharp inward pointing apex (i.e., inverted cone). We note, however, that sizable electromagnetic field enhancements can occur at the boundary between the pinhole defect and the shell surface, if the connecting edge is significantly sharper (i.e., < 1 nm) than experimentally inferred and presently modeled.

As a third hot spot model geometry, we examine outward-facing, conical asperities with a rounded tip of radius r_A, cone half angle θ = 30°, and height h = 5 nm, as shown in Figure 13(c). This is modeled as two spheres of differing radius at the same potential, a geometry often used to explain the "corona effect" around sharp metal points. As expected, $(|\mathbf{E}|/|\mathbf{E}_0|)_{MAX}$ around such a conical asperity increases dramatically with a decrease in tip radius r_A [Figure 13(c); black circles], in fact, rapidly enough to offset the corresponding reduction in emitter area ($\propto r_A^2$) [Figure 13(c); red squares]. This defect geometry is one that could possibly enhance Au nanoshell photoemission by multiple orders of magnitude, even though it is dimensionally too small to identify in SEM, consistent with our experimental observations.

While conical asperities could in principle explain many experimental observations, it is difficult to reconcile formation of such nanoscopically sharp outward features with the growth mechanism of silica–Au core–shell species. Specifically, silica cores are initially decorated with Au nanospheres a few nanometers in diameter that act as embryonic "seeds" for subsequent growth and merger of Au^{3+}. Whereas formation of outward conical asperities via such a mechanism seems unlikely, inward facing crevices formed at the intersection of two or more accreting plates would be a much more plausible choice. As a fourth possible hot spot geometry, we thus consider "nanocrevices" on the Au nanoshell surfaces formed in the gap between two spherical asperities, as depicted in Figure 13(d). For the purposes of COMSOL calculations, two spheres are separated by a small gap g and are constrained to protrude a height h above the shell surface and meet at an angle θ. Of the three structural parameters defining this geometry, we focus specifically on the dominating effect of the gap size on the local field enhancement.

As shown in Figure 13(d), narrower interasperity gaps, g, lead to progressively larger $(|\mathbf{E}|/|\mathbf{E}_0|)_{MAX}$ values (black circles), in analogy with the outward-facing conical asperities discussed previously. Most relevantly, these sharp crevice-like hot spots give rise to near-field enhancements that increase sufficiently rapidly with decreasing effective emitter area to maintain high photoelectron yield [Figure 13(d)]. With defects of this geometry on the nanoshell surface, the photoemissivity could be completely dominated by features too small to identify in SEM images. In addition, since different structural parameters (g, θ, h) defining a nanocrevice result in quite different local $|\mathbf{E}|/|\mathbf{E}_0|$ values, one would also expect substantial particle-to-particle inhomogeneity in multiphoton photoemissivity when defects of this type are present, in qualitative agreement with the observed 10^5-fold differences between the weakest and strongest photoemitting nanoshells.

Nanocrevices have long been known to yield large near-field enhancements and have actually been postulated to explain early observations of molecular SERS on thin metal films.[66−72] In subsequent work on individual plasmonic nanostructures, enormous SERS enhancements observed in particle aggregates were attributed to the extremely high electromagnetic near fields in the gaps between particles.[30,31,73,74] Interestingly, the substantial near-field enhancements of nanocrevices have received less attention, yet may be the prime contributor to the anomalously strong enhancements on Au nanoshells

dx.doi.org/10.1021/jp407424n | J. Phys. Chem. C 2013, 117, 22545−22559

observed in our experiments. This is consistent with the fact that nanocrevices may be quite prevalent on nanoshell surfaces, depending on the specifics of Au nanoshell growth and postsynthetic ripening conditions.[48,75]

From these studies it is apparent that Au nanoshells may offer some distinct advantages as potential SERS substrates. The formation of crevice-like hot spots on their surfaces can be a frequent consequence of either their initial preparation or their subsequent Ostwald ripening. Through appropriate modification of either the growth or postsynthetic conditions, it may be possible to (i) introduce higher densities of these features and/or (ii) tailor the hot spot morphology to provide even further enhancements of the near field. Since enhancement factors depend on local hot spot morphology, while the plasmon frequency relies almost exclusively on global nanostructure parameters (i.e., r_1 and r_2), one could envision independently tuning the magnitude of $|\mathbf{E}|/|\mathbf{E}_0|$ and its spectral response by controllable introduction of crevice-like defects onto the Au nanoshell surface.

As a final comment, we return to the dramatic changes in photoemissivity routinely observed for single Au nanoshells. Two types of changes are observed: (i) a 10- to 100-fold *increase* in photoemissivity at relatively low laser intensities ($I \sim 1-4 \times 10^8$ W/cm^2), followed by (ii) a subsequent *decrease* of photoelectron yield at a higher photon flux ($I \sim 5 \times 10^9$ W/cm^2). Both processes show strong dependence on excitation laser polarization, suggesting that hot spot, rather than particle-wide, changes in particle structure/environment lead to the observed behavior. As a result, neither thermally driven modifications to the particle nor improved electrical contacts with the substrate are likely responsible. This is further supported by the small particle temperature increases of $\Delta T \sim 1$ and 20 K estimated for excitation conditions (i) and (ii), respectively. Instead, the process(es) leading to local changes in the particle structure/environment must be either (i) electric field or (ii) photocurrent induced.

To explore the possibility of electric field-driven rearrangements, we estimate the electric field magnitude around a strongly near-field enhancing hot spot, for which $|\mathbf{E}|/|\mathbf{E}_0| \sim 50$ are generally inferred. At laser intensities where significant changes in polarization-dependent photoemission are first observed ($I \sim 5 \times 10^9$ W/cm^2), the incident electromagnetic radiation amounts to $|\mathbf{E}_0| \sim 0.2$ V/nm, translating into an enhanced field of $|\mathbf{E}| \sim 10$ V/nm. By way of comparison, electric fields in typical covalent or ionic bonds range from $|\mathbf{E}_{bond}| \sim 20$ to 100 V/nm, i.e., which indicates that the electric field of a plasmon could induce chemical reactions/surface rearrangements, particularly at higher excitation intensities. More generally, plasmon-driven chemistry is currently a matter of intense research with several underlying mechanisms currently proposed.[75−81]

Alternatively, the observed changes in nanoparticle photoemissivity could arise from photocurrent-induced effects, for example, (i) ligand desorption/ionization, (ii) Au surface/crystalline structure rearrangement, (iii) or even emission of charged atomic gold species. Interestingly, we do observe evidence for the latter process at significantly higher $I \sim 7.4 \times 10^{10}$ W/cm^2 (i.e., $|\mathbf{E}| \sim 37$ V/nm), where cationic species are detected on the channeltron and which exhibit a laser polarization dependence coincident with that of the photoelectrons. However, these processes are not expected at $I \sim 1-4 \times 10^8$ W/cm^2 (i.e., $|\mathbf{E}| \sim 1$ V/nm), where the dramatic changes in particle photoemissivity are first observed.

We instead speculate that the emitted electrons locally interact with the adsorbed molecular species in a way that initially enhances the overall photoelectron yield, perhaps via local removal of the capping ligand layer around a hot spot. Interestingly, surprisingly little is known about the chemistry and transport efficiency of such low kinetic energy electrons (few eV) through thin molecular films,[82,83] despite the corresponding wealth of literature for higher-energy electrons.[84] Nevertheless, experimental observations indicate that low KE electron collisions induce single- and double-strand breaks in DNA, which might suggest a similarly strong interaction with other organic materials.[85−88] Indeed, this is further supported by groundbreaking studies by Naaman and co-workers, whereby interactions of ballistic low KE electrons with chiral molecular adlayers have been shown to result in electron emission with high degrees of spin polarization.[89,90] However, further studies will be necessary to determine whether such slow electron−ligand interactions at the surface of Au nanoshells are ultimately responsible for the observed dramatic changes in multiphoton photoemissivity.

V. CONCLUSIONS

Surprisingly intense four-photon photoelectron emission from individual, supported Au nanoshells has been observed upon plasmon resonant ultrafast excitation with $\lambda = 700-900$ nm photons. The strong $\cos^8(\theta)$ sensitivity of the photoemission signal on excitation laser polarization angle θ implies the existence of high near-field enhancement areas on the nanoshell surface, with local field enhancements in excess of $|\mathbf{E}|/|\mathbf{E}_0| \sim 50$ inferred around some of these hot spots from the measured particle photoemissivities. Numerical simulations of the electric fields for various hot spot morphologies indicate nanocrevices in the Au nanoshell surfaces as a plausible source of large near-field enhancements. These structural features arise at the intersection of growing seed nanoparticles during Au nanoshell synthesis and are consequently expected to be present in large numbers. The finding bears important implications for potential use of Au nanoshells in SERS due to their unique capability to tune both the magnitude and the spectral dependence of local field enhancement nearly independently, through introduction of nanocrevices of controlled number and geometry onto the nanoshell surface.

AUTHOR INFORMATION

Corresponding Authors

*Tel.: (303) 492-8857. E-mail: djn@jila.colorado.edu.
*Tel.: (713) 348-5746. E-mail: halas@rice.edu.

Notes

The authors declare no competing financial interest.

ACKNOWLEDGMENTS

This work has been supported by the Air Force Office of Scientific Research (FA9550-12-1-0139), with additional funds for optics, microscopy, and computer resources provided by the National Science Foundation (CHE1012685, PHYS1125844) and the National Institute for Standards and Technology. NJH and SM were supported by the Robert A. Welch Foundation under grant C-1220, the Office of Naval Research under grant N00014-10-1-0989, the DoD NSSEFF (N00244-09-1-0067), and the U.S. Army Research Laboratory and Office under contract/grant number WF911NF-12-1-0407. We also gratefully acknowledge D. Alchenberger for help with the SEM

instrumentation, and Ciceron Ayala-Orozco for nanoparticle synthesis.

REFERENCES

(1) El-Sayed, M. A. Some Interesting Properties of Metals Confined in Time and Nanometer Space of Different Shapes. *Acc. Chem. Res.* **2001**, *34* (4), 257−264.
(2) Kelly, K. L.; Coronado, E.; Zhao, L. L.; Schatz, G. C. The Optical Properties of Metal Nanoparticles: The Influence of Size, Shape, and Dielectric Environment. *J. Phys. Chem. B* **2003**, *107* (3), 668−677.
(3) Lee, K.-S.; El-Sayed, M. A. Gold and Silver Nanoparticles in Sensing and Imaging: Sensitivity of Plasmon Response to Size, Shape, and Metal Composition. *J. Phys. Chem. B* **2006**, *110*, 19220−19225.
(4) Ringe, E.; McMahon, J. M.; Sohn, K.; Cobley, C. M.; Xia, Y.; Huang, J.; Schatz, G. C.; Marks, L. D.; Van Duyne, R. P. Unraveling the Effects of Size, Composition, and Substrate on the Localized Surface Plasmon Resonance Frequencies of Gold and Silver Nanocubes: A Systematic Single-Particle Approach. *J. Phys. Chem. C* **2010**, *114*, 12511−12516.
(5) Wiley, B. J.; Im, S. H.; Li, Z.-Y.; McLellen, J.; Siekkinen, A.; Xia, Y. Maneuvering the Surface Plasmon Resonance of Silver Nanostructures through Shape-Controlled Synthesis. *J. Phys. Chem. B* **2006**, *110*, 15666−15675.
(6) Ringe, E.; Langille, M. R.; Sohn, K.; Zhang, J.; Huang, J. X.; Mirkin, C. A.; Van Duyne, R. P.; Marks, L. D. Plasmon Length: A Universal Parameter to Describe Size Effects in Gold Nanoparticles. *J. Phys. Chem. Lett.* **2012**, *3* (11), 1479−1483.
(7) Sau, T. K.; Rogach, A. L.; Jackel, F.; Klar, T. A.; Feldmann, J. Properties and Applications of Colloidal Nonspherical Noble Metal Nanoparticles. *Adv. Mater.* **2010**, *22* (16), 1805−1825.
(8) Turkevich, J.; Stevenson, P. C.; Hillier, J. A Study of the Nucleation and Growth Processes in the Synthesis of Colloidal Gold. *Discuss. Faraday Soc.* **1951**, *11*, 55−75.
(9) Frens, G. Controlled Nucleation for Regulation of Particle-Size in Monodisperse Gold Suspensions. *Nat. Phys. Sci.* **1973**, *241* (105), 20−22.
(10) Nikoobakht, B.; El-Sayed, M. A. Preparation and Growth Mechanism of Gold Nanorods (NRs) Using Seed-Mediated Growth Method. *Chem. Mater.* **2003**, *15* (10), 1957−1962.
(11) Sun, Y. G.; Xia, Y. N. Shape-Controlled Synthesis of Gold and Silver Nanoparticles. *Science* **2002**, *298* (5601), 2176−2179.
(12) Jin, R. C.; Cao, Y. W.; Mirkin, C. A.; Kelly, K. L.; Schatz, G. C.; Zheng, J. G. Photoinduced Conversion of Silver Nanospheres to Nanoprisms. *Science* **2001**, *294* (5548), 1901−1903.
(13) Sanchez-Iglesias, A.; Pastoriza-Santos, I.; Perez-Juste, J.; Rodriguez-Gonzalez, B.; de Abajo, F. J. G.; Liz-Marzan, L. M. Synthesis and Optical Properties of Gold Nanodecahedra with Size Control. *Adv. Mater.* **2006**, *18* (19), 2529−2534.
(14) Skrabalak, S. E.; Au, L.; Li, X. D.; Xia, Y. N. Facile synthesis of Ag nanocubes and Au nanocages. *Nat. Protoc.* **2007**, *2* (9), 2182−2190.
(15) Oldenburg, S. J.; Averitt, R. D.; Westcott, S. L.; Halas, N. J. Nanoengineering of Optical Resonances. *Chem. Phys. Lett.* **1998**, *288* (2−4), 243−247.
(16) Mie, G. Articles on the Optical Characteristics of Turbid Tubes, Especially Colloidal Metal Solutions. *Ann. Phys. (Berlin, Ger.)* **1908**, *25* (3), 377−445.
(17) Aden, A. L.; Kerker, M. Scattering of Electromagnetic Waves from 2 Concentric Spheres. *J. Appl. Phys.* **1951**, *22* (10), 1242−1246.
(18) Prodan, E.; Radloff, C.; Halas, N. J.; Nordlander, P. A hybridization model for the plasmon response of complex nanostructures. *Science* **2003**, *302* (5644), 419−422.
(19) Linic, S.; Christopher, P.; Ingram, D. B. Plasmonic-metal nanostructures for efficient conversion of solar to chemical energy. *Nat. Mater.* **2011**, *10* (12), 911−921.
(20) Atwater, H. A.; Polman, A. Plasmonics for Improved Photovoltaic Devices. *Nat. Mater.* **2010**, *9* (3), 205−213.
(21) Pillai, S.; Catchpole, K. R.; Trupke, T.; Green, M. A. Surface Plasmon Enhanced Silicon Solar Cells. *J. Appl. Phys.* **2007**, *101* (9), 093105.
(22) Cole, J. R.; Mirin, N. A.; Knight, M. W.; Goodrich, G. P.; Halas, N. J. Photothermal Efficiencies of Nanoshells and Nanorods for Clinical Therapeutic Applications. *J. Phys. Chem. C* **2009**, *113* (28), 12090−12094.
(23) Skrabalak, S. E.; Chen, J. Y.; Sun, Y. G.; Lu, X. M.; Au, L.; Cobley, C. M.; Xia, Y. N. Gold Nanocages: Synthesis, Properties, and Applications. *Acc. Chem. Res.* **2008**, *41* (12), 1587−1595.
(24) Huschka, R.; Barhoumi, A.; Liu, Q.; Roth, J. A.; Ji, L.; Halas, N. J. Gene Silencing by Gold Nanoshell-Mediated Delivery and Laser-Triggered Release of Antisense Oligonucleotide and siRNA. *ACS Nano* **2012**, *6* (9), 7681−7691.
(25) Wustholz, K. L.; Henry, A.-I.; McMahon, J. M.; Freeman, R. G.; Valley, N.; Piotti, M. E.; Natan, M. J.; Schatz, G. C.; Van Duyne, R. P. Structure-Activity Relationships in Gold Nanoparticle Dimers and Trimers for Surface-Enhanced Raman Spectroscopy. *J. Am. Chem. Soc.* **2012**, *132*, 10903−10910.
(26) Giannini, V.; Fernández-Domínguez, A. I.; Heck, S. C.; Maier, S. A. Plasmonic Nanoantennas: Fundamentals and Their Use in Controlling the Radiative Properties of Nanoemitters. *Chem. Rev.* **2011**, *111*, 3888−3912.
(27) Large, N.; Abb, M.; Aizpurua, J.; Muskens, O. L. Photoconductively Loaded Plasmonic Nanoantenna as Building Block for Ultracompact Optical Switches. *Nano Lett.* **2010**, *10*, 1741−1746.
(28) Brown, L. V.; Sobhani, H.; Lassiter, J. B.; Nordlander, P.; Halas, N. J. Heterodimers: Plasmonic Properties of Mismatched Nanoparticle Pairs. *ACS Nano* **2010**, *4* (2), 819−832.
(29) Lassiter, J. B.; Aizpurua, J.; Hernandez, L. I.; Brandl, D. W.; Romero, I.; Lal, S.; Hafner, J. H.; Nordlander, P.; Halas, N. J. Close encounters between two nanoshells. *Nano Lett.* **2008**, *8* (4), 1212−1218.
(30) Michaels, A. M.; Jiang, J.; Brus, L. Ag nanocrystal junctions as the site for surface-enhanced Raman scattering of single Rhodamine 6G molecules. *J. Phys. Chem. B* **2000**, *104* (50), 11965−11971.
(31) Dieringer, J. A.; Lettan, R. B.; Scheidt, K. A.; Van Duyne, R. P. A frequency domain existence proof of single-molecule surface-enhanced Raman Spectroscopy. *J. Am. Chem. Soc.* **2007**, *129* (51), 16249−16256.
(32) Talley, C. E.; Jackson, J. B.; Oubre, C.; Grady, N. K.; Hollars, C. W.; Lane, S. M.; Huser, T. R.; Nordlander, P.; Halas, N. J. Surface-Enhanced Raman Scattering from Individual Au Nanoparticles and Nanoparticle Dimer Substrates. *Nano Lett.* **2005**, *5* (8), 1569−1574.
(33) Schweikhard, V.; Grubisic, A.; Baker, T. A.; Nesbitt, D. J. Multiphoton Scanning Photoionization Imaging Microscopy for Single-Particle Studies of Plasmonic Metal Nanostructures. *J. Phys. Chem. C* **2011**, *115* (1), 83−91.
(34) Schweikhard, V.; Grubisic, A.; Baker, T. A.; Thomann, I.; Nesbitt, D. J. Polarization-Dependent Scanning Photoionization Microscopy: Ultrafast Plasmon-Mediated Electron Ejection Dynamics in Single Au Nanorods. *ACS Nano* **2011**, *5* (5), 3724−3735.
(35) Grubisic, A.; Ringe, E.; Cobley, C. M.; Xia, Y.; Marks, L. D.; Van Duyne, R. P.; Nesbitt, D. J. Plasmonic Near-Electric Field Enhancement Effects in Ultrafast Photoelectron Emission: Correlated Spatial and Laser Polarization Microscopy Studies of Individual Ag Nanocubes. *Nano Lett.* **2012**, *12* (9), 4823−4829.
(36) Grubisic, A.; Schweikhard, V.; Baker, T. A.; Nesbitt, D. J. Coherent Multiphoton Photoelectron Emission from Single Au Nanorods: The Critical Role of Plasmonic Electric Near-Field Enhancement. *ACS Nano* **2013**, *7* (1), 87−99.
(37) Petek, H.; Ogawa, S. Femtosecond Time-Resolved Two-Photon Photoemission Studies of Electron Dynamics in Metals. *Prog. Surf. Sci.* **1998**, *56* (4), 239−310.
(38) Bovensiepen, U.; Declair, S.; Lisowski, M.; Loukakos, P. A.; Hotzel, A.; Richter, M.; Knorr, A.; Wolf, M. Ultrafast Electron Dynamics in Metals: Real-Time Analysis of a Reflected Light Field Using Photoelectrons. *Phys. Rev. B* **2009**, *79* (4), 045415.

(39) Bisio, F.; Nyvlt, M.; Franta, J.; Petek, H.; Kirschner, J. Mechanisms of High-Order Perturbative Photoemission from Cu(001). *Phys. Rev. Lett.* **2006**, *96* (8), 087601.
(40) Winkelmann, A.; Lin, W. C.; Chiang, C. T.; Bisio, F.; Petek, H.; Kirschner, J. Resonant Coherent Three-Photon Photoemission from Cu(001). *Phys. Rev. B* **2009**, *80* (15), 155128.
(41) Kruger, M.; Schenk, M.; Forster, M.; Hommelhoff, P. Attosecond Physics in Photoemission from a Metal Nanotip. *J. Phys. B: At. Mol. Opt. Phys.* **2012**, *45* (7), 074006.
(42) Gudde, J.; Rohleder, M.; Meier, T.; Koch, S. W.; Hofer, U. Time-Resolved Investigation of Coherently Controlled Electric Currents at a Metal Surface. *Science* **2007**, *318* (5854), 1287−1291.
(43) Michaelson, H. B. Work Function of Elements and its Periodicity. *J. Appl. Phys.* **1977**, *48* (11), 4729−4733.
(44) Hrelescu, C.; Sau, T. K.; Rogach, A. L.; Jackel, F.; Laurent, G.; Douillard, L.; Charra, F. Selective Excitation of Individual Plasmonic Hotspots at the Tips of Single Gold Nanostars. *Nano Lett.* **2011**, *11* (2), 402−407.
(45) Cinchetti, M.; Gloskovskii, A.; Nepjiko, S. A.; Schonhense, G.; Rochholz, H.; Kreiter, M. Photoemission Electron Microscopy As a Tool for the Investigation of Optical Near Fields. *Phys. Rev. Lett.* **2005**, *95* (4), 047601.
(46) Schertz, F.; Schmelzeisen, M.; Mohammadi, R.; Kreiter, M.; Elmers, H. J.; Schonhense, G. Near Field of Strongly Coupled Plasmons: Uncovering Dark Modes. *Nano Lett.* **2012**, *12* (4), 1885−1890.
(47) Peppernick, S. J.; Joly, A. G.; Beck, K. M.; Hess, W. P. Plasmonic field enhancement of individual nanoparticles by correlated scanning and photoemission electron microscopy. *J. Chem. Phys.* **2011**, *134*, 3.
(48) Brinson, B. E.; Lassiter, J. B.; Levin, C. S.; Bardhan, R.; Mirin, N.; Halas, N. J. Nanoshells Made Easy: Improving Au Layer Growth on Nanoparticle Surfaces. *Langmuir* **2008**, *24* (24), 14166−14171.
(49) Duff, D. G.; Baiker, A.; Edwards, P. P. A New Hydrosol of Gold Clusters 0.1. Formation and Particle-size Variation. *Langmuir* **1993**, *9* (9), 2301−2309.
(50) Link, S.; Mohamed, M. B.; El-Sayed, M. A. Simulation of the Optical Absorption Spectra of Gold Nanorods as a Function of their Aspect Ratio and the Effect of the Medium Dielectric Constant. *J. Phys. Chem. B* **1999**, *103* (16), 3073−3077.
(51) Miller, M. M.; Lazarides, A. A. Sensitivity of metal nanoparticle surface plasmon resonance to the dielectric environment. *J. Phys. Chem. B* **2005**, *109* (46), 21556−21565.
(52) Templeton, A. C.; Pietron, J. J.; Murray, R. W.; Mulvaney, P. Solvent refractive index and core charge influences on the surface plasmon absorbance of alkanethiolate monolayer-protected gold clusters. *J. Phys. Chem. B* **2000**, *104* (3), 564−570.
(53) Chen, H. J.; Kou, X. S.; Yang, Z.; Ni, W. H.; Wang, J. F. Shape- and Size-dependent Refractive Index Sensitivity of Gold Nanoparticles. *Langmuir* **2008**, *24* (10), 5233−5237.
(54) Grady, N. K.; Halas, N. J.; Nordlander, P. Influence of Dielectric Function Properties on the Optical Response of Plasmon Resonant Metallic Nanoparticles. *Chem. Phys. Lett.* **2004**, *399* (1−3), 167−171.
(55) Knight, M. W.; Wu, Y. P.; Lassiter, J. B.; Nordlander, P.; Halas, N. J. Substrates Matter: Influence of an Adjacent Dielectric on an Individual Plasmonic Nanoparticle. *Nano Lett.* **2009**, *9* (5), 2188−2192.
(56) Grubisic, A.; Schweikhard, V.; Baker, T. A.; Nesbitt, D. J. Multiphoton Photoelectron Emission Microscopy of Single Au Nanorods: Combined Experimental and Theoretical Study of Rod Morphology and Dielectric Environment on Localized Surface Plasmon Resonances. *Phys. Chem. Chem. Phys.* **2013**, *15*, 10616−10627.
(57) Monti, O. L. A.; Baker, T. A.; Nesbitt, D. J. Imaging Nanostructures with Scanning Photoionization Microscopy. *J. Chem. Phys.* **2006**, *125* (15), 154709.
(58) Henry, A. I.; Bingham, J. M.; Ringe, E.; Marks, L. D.; Schatz, G. C.; Van Duyne, R. P. Correlated Structure and Optical Property Studies of Plasmonic Nanoparticles. *J. Phys. Chem. C* **2011**, *115* (19), 9291−9305.
(59) Knight, M. W.; Halas, N. J. Nanoshells to nanoeggs to nanocups: optical properties of reduced symmetry core-shell nanoparticles beyond the quasistatic limit. *New J. Phys.* **2008**, *10*.
(60) Johnson, P. B.; Christy, R. W. Optical-Constants of Noble-Metals. *Phys. Rev. B* **1972**, *6* (12), 4370−4379.
(61) Tsang, T.; Srinivasanrao, T.; Fischer, J. Surface-Plasmon Field-Enhanced Multiphoton Photoelectric-Emission From Metal-Films. *Phys. Rev. B* **1991**, *43* (11), 8870−8878.
(62) Protsenko, I. E.; Uskov, A. V. Photoemission from metal nanoparticles. *Phys. Usp.* **2012**, *55* (5), 508−518.
(63) Yalunin, S. V.; Gulde, M.; Ropers, C. Strong-Field Photoemission from Surfaces: Theoretical Approaches. *Phys. Rev. B* **2011**, *84* (19), 195426.
(64) Sonnichsen, C.; Franzl, T.; Wilk, T.; von Plessen, G.; Feldmann, J.; Wilson, O.; Mulvaney, P. Drastic Reduction of Plasmon Damping in Gold Nanorods. *Phys. Rev. Lett.* **2002**, *88* (7), 077402.
(65) Nehl, C. L.; Grady, N. K.; Goodrich, G. P.; Tam, F.; Halas, N. J.; Hafner, J. H. Scattering Spectra of Single Gold Nanoshells. *Nano Lett.* **2004**, *4* (12), 2355−2359.
(66) Garcia-Vidal, F. J.; Pendry, J. B. Collective theory for surface enhanced Raman scattering. *Phys. Rev. Lett.* **1996**, *77* (6), 1163−1166.
(67) Weber, M.; Mills, D. L. Interaction of Electromagnetic-waves with Periodic Gratings - Enhanced Fields and the Reflectivity. *Phys. Rev. B* **1983**, *27* (5), 2698−2709.
(68) Wirgin, A.; Lopezrios, T. Can Surface-enhanced Raman-scattering Be Caused by Waveguide Resonances. *Opt. Commun.* **1984**, *48* (6), 416−420.
(69) Jha, S. S.; Kirtley, J. R.; Tsang, J. C. Intensity of Raman-scattering from Molecules Adsorbed on a Metallic Grating. *Phys. Rev. B* **1980**, *22* (8), 3973−3982.
(70) Moskovits, M. Surface-roughness and Enhanced Intensity of Raman-scattering by Molecules Adsorbed on Metals. *J. Chem. Phys.* **1978**, *69* (9), 4159−4161.
(71) Cotton, T. M.; Schultz, S. G.; Vanduyne, R. P. Surface-enhanced Resonance Raman-scattering from Cytochrome-C and Myoglobin Adsorbed on a Silver Electrode. *J. Am. Chem. Soc.* **1980**, *102* (27), 7960−7962.
(72) Creighton, J. A.; Albrecht, M. G.; Hester, R. E.; Matthew, J. A. D. Dependence of Intensity of Raman Bands of Pyridine at a Silver Electrode on Wavelength of Excitation. *Chem. Phys. Lett.* **1978**, *55* (1), 55−58.
(73) Moskovits, M.; Jeong, D. H. Engineering nanostructures for giant optical fields. *Chem. Phys. Lett.* **2004**, *397* (1−3), 91−95.
(74) McMahon, J. M.; Henry, A.-I.; Wustholz, K. L.; Natan, M. J.; Freeman, G.; Van Duyne, R. P.; Schatz, G. C. Gold Nanoparticle Dimer Plasmonics: Finite Element Method Calculations of the Electromagnetic Enhancement to Surface-Enhanced Raman Spectroscopy. *Anal. Bioanal. Chem.* **2009**, *394*, 1819−1825.
(75) Brus, L. Noble Metal Nanocrystals: Plasmon Electron Transfer Photochemistry and Single-Molecule Raman Spectroscopy. *Acc. Chem. Res.* **2008**, *41* (12), 1742−1749.
(76) Mukherjee, S.; Libisch, F.; Large, N.; Neumann, O.; Brown, L. V.; Cheng, J.; Lassiter, J. B.; Carter, E. A.; Nordlander, P.; Halas, N. J. Hot Electrons Do the Impossible: Plasmon-Induced Dissociation of H2 on Au. *Nano Lett.* **2012**, *13* (1), 240−247.
(77) Thomann, I.; Pinaud, B. A.; Chen, Z.; Clemens, B. M.; Jaramillo, T. F.; Brongersma, M. L. Plasmon Enhanced Solar-to-Fuel Energy Conversion. *Nano Lett.* **2011**, *11* (8), 3440−3446.
(78) Linic, S.; Christopher, P.; Xin, H.; Marimuthu, A. Catalytic and Photocatalytic Transformations on Metal Nanoparticles with Targeted Geometric and Plasmonic Properties. *Acc. Chem. Res.* **2013**, *46*, 1890−1899.
(79) Lee, J.; Mubeen, S.; Ji, X.; Stucky, G. D.; Moskovits, M. Plasmonic Photoanodes for Solar Water Splitting with Visible Light. *Nano Lett.* **2012**, *12* (9), 5014−5019.
(80) Mubeen, S.; Lee, J.; Singh, N.; Kramer, S.; Stucky, G. D.; Moskovits, M. An autonomous photosynthetic device in which all charge carriers derive from surface plasmons. *Nat. Nano* **2013**, *8* (4), 247−251.

(81) Huschka, R.; Zuloaga, J.; Knight, M. W.; Brown, L. V.; Nordlander, P.; Halas, N. J. Light-Induced Release of DNA from Gold Nanoparticles: Nanoshells and Nanorods. *J. Am. Chem. Soc.* **2011**, *133* (31), 12247−12255.
(82) Naaman, R.; Vager, Z. Electron transmission through organized organic thin films. *Acc. Chem. Res.* **2003**, *36* (5), 291−299.
(83) Naaman, R.; Sanche, L. Low-energy electron transmission through thin-film molecular and biomolecular solids. *Chem. Rev.* **2007**, *107* (5), 1553−1579.
(84) Seah, M. P.; Dench, W. A. Quantitative electron spectroscopy of surfaces: A standard data base for electron inelastic mean free paths in solids. *Surf. Interface Anal.* **1979**, *1* (1), 2−11.
(85) Boudaiffa, B.; Cloutier, P.; Hunting, D.; Huels, M. A.; Sanche, L. Resonant formation of DNA strand breaks by low-energy (3 to 20 eV) electrons. *Science* **2000**, *287* (5458), 1658−1660.
(86) Li, X. F.; Sevilla, M. D.; Sanche, L. Density functional theory studies of electron interaction with DNA: Can zero eV electrons induce strand breaks? *J. Am. Chem. Soc.* **2003**, *125* (45), 13668−13669.
(87) Berdys, J.; Anusiewicz, I.; Skurski, P.; Simons, J. Damage to model DNA fragments from very low-energy (< 1 eV) electrons. *J. Am. Chem. Soc.* **2004**, *126* (20), 6441−6447.
(88) Ray, S. G.; Daube, S. S.; Naaman, R. On the capturing of low-energy electrons by DNA. *Proc. Natl. Acad. Sci. U.S.A.* **2005**, *102* (1), 15−19.
(89) Gohler, B.; Hamelbeck, V.; Markus, T. Z.; Kettner, M.; Hanne, G. F.; Vager, Z.; Naaman, R.; Zacharias, H. Spin Selectivity in Electron Transmission Through Self-Assembled Monolayers of Double-Stranded DNA. *Science* **2011**, *331* (6019), 894−897.
(90) Xie, Z. T.; Markus, T. Z.; Cohen, S. R.; Vager, Z.; Gutierrez, R.; Naaman, R. Spin Specific Electron Conduction through DNA Oligomers. *Nano Lett.* **2011**, *11* (11), 4652−4655.